4
Autogenous Welding Techniques

This chapter focuses on autogenous welding techniques to fabricate the dissimilar weld joint (DWJ) between P91 steel and Incoloy 800HT. The autogenous welding techniques involved were laser beam welding (LBW), electron beam welding (EBW), and autogenous tungsten inert gas (TIG) welding processes. In-depth characterization was carried out for different welded plates in order to address the strength and concerns related to the mentioned welding techniques.

4.1 Laser Beam Welding (LBW)

4.1.1 Macroscopic Observations

This investigation attempts to explore the weld characteristics of a laser-welded dissimilar joint of P91 steel and Incoloy 800HT alloy. In critical operating conditions, it is essential for a dissimilar joint to preserve its characteristics and be free from any kind of defect. The difference between the physical properties of P91 and Incoloy 800HT makes their weldability challenging. Thus, the need for a detailed characterization of this dissimilar weld arises. The single-pass laser welding technique was employed to obtain maximum penetration through the keyhole mode. The macro-optical examination (Figure 4.1) shows the complete penetrations with no inclusion and no porosities in the weld. The weld bead is narrow and shaped like a keyhole. In the weld center, the weld bead was only 1.28 mm wide, while at the weld top face, it was around 3.24 mm wide. The macrograph of the weld cross-section representing the weld bead geometry in Figure 4.1 hints at the keyhole mode of penetration caused by vapor pressure under high heat energy input in laser welding. Complete penetration with a narrow weld bead was obtained as per the macrograph. Due to heat transfer and conduction, a grain size gradient was formed along the weldments.

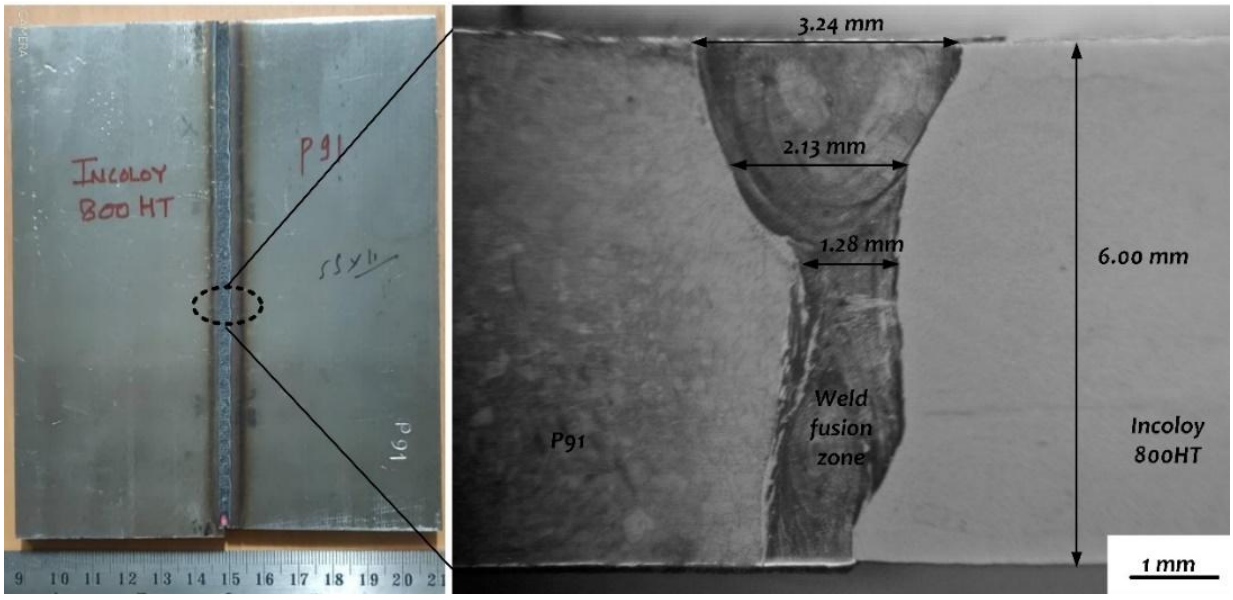


Figure 4.1 : Macrograph of the laser weld bead

4.1.2 Heat Affected Zone (HAZ) Microstructure Characterization

The micrograph of the P91 steel HAZ next to the WFZ consists of three different regions having an inhomogeneous microstructure. On the basis of the peak temperature experienced and phase transformations during the weld thermal cycle, the P91 HAZ typically consists of the coarse grained HAZ (CGHAZ), fine grained HAZ (FGHAZ), and inter critical HAZ (ICHAZ) (Mayr and Cerjak, 2010). The microstructure of the CGHAZ adjacent to the WFZ experiences a peak temperature much higher than the Ac3, and due to exposure at such a high temperature, precipitates dissolved, which contributes to the reduction of pinning force at grain boundaries and results in grain coarsening, as shown in Figure 4.2(a). The optical image Figure 4.2(a) shows the presence of the lath blocks and coarse grains in CGHAZ. The grain size observed in the CGHAZ was around 25 ± 5 μm. The regions of FGHAZ and ICHAZ both have fine-grain structures and were difficult to distinguish by optical image, as shown in Figure 4.2(b-d). However, the peak temperature experienced by the FGHAZ was higher or close to $A_{c3,}$ and for ICHAZ, it was in the range of A_{c1} to A_{c3}. That difference in peak temperature experienced by the FGHAZ/ICHAZ leads to the variation in the overall fraction area of the precipitates and final microstructure. FGHAZ exhibits the untempered martensitic microstructure and partial dissolution of the carbide precipitates due to the lower peak temperature and results in the formation of fine prior austenite grain boundaries (PAGs) compared to CGHAZ Figure 4.2(b). The grain size observed in the FGHAZ was around 8 ± 5 μm. In ICHAZ, the lower peak temperature results in the partial transformation of the austenite and negligible dissolution of the carbide precipitates. That results in the final ICHAZ microstructure exhibiting the complex structure of the untempered martensite and austenite transform products (ATP), as shown in Figure 4.2(c). The grain size observed in the ICHAZ was around 8 ± 5 μm. Although all the regions of P91 HAZ of the weldments differ significantly in their PAGs, fraction area of the precipitates, and final microstructure, however after PWHT, the phase of each zone was basically the same and consisted of the ferritic-carbide mixture, i.e., tempered martensite and carbide precipitates with different tempering degree depending on their peak temperature experienced during the welding cycle. The region of the HAZs of P91 steel after the PWHT is shown in Figure 4.2(d-f). After PWHT, however, more precipitates were evolved at grain boundaries and matrix. This caused softening across HAZ due to a reduction in solid solution hardening (Pandey et al., 2019a). The CGHAZ after PWHT exhibits the coarse PAGs in the tempered martensitic matrix (Figure 4d: optical image) along with newly evolved carbide and carbonitrides precipitates along the boundaries and inside the matrix (Figure 4.2(d)). The evolution of the new precipitates was also observed in FGHAZ and ICHAZ, as given in Figure 4.2(e-f). The higher magnification SE image was captured in the ICHAZ for both AW (Figure 4.2(g)) and PWHT (Figure 4.2(h)) conditions to observe the decoration of the particles along the boundaries and inside the matrix. The image also shows the morphology and distribution of the precipitates inside the matrix and is also utilized for the EDS spectrum. The EDS spectrum of the white particles (Figure 4.2(g): AW) decorated along the PAGBs shows the higher weight percentage of the Cr (16.52%) and Mo (2.85%), which ensures the presence of the secondary phase carbide particles enriched with Cr and Mo. The white particles inside the matrix show chromium (Cr) and molybdenum (Mo) as major elements, along with vanadium (V) and niobium (Nb). The EDS spectrum of the matrix is represented at point 3. A similar observation was also observed after the PWHT and represented in Figure 4.2(h). It is also well known from other studies that P91 steel contains mainly intragranular MX precipitates enriched with V and Nb, and intergranular $M_{23}C_6$ precipitates at PAGBs and sub-grain boundaries mainly enriched with Cr and Mo.

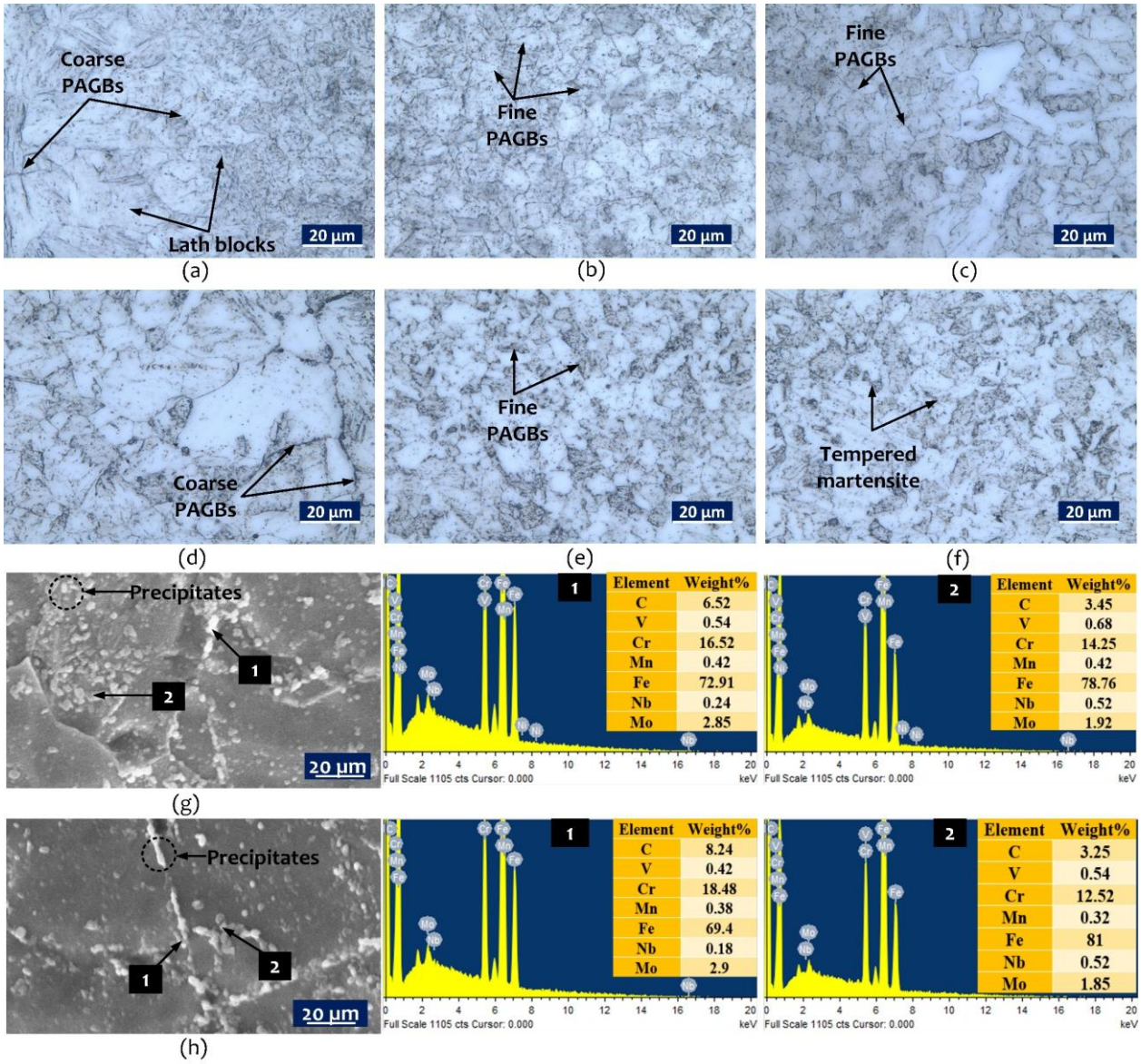


Figure 4.2 : P91 HAZs in AW condition: (a) CGHAZ (b) FGHAZ (c) ICHAZ; after PWHT (d) CGHAZ (e) FGHAZ (f) ICHAZ; ICHAZ at higher magnification showing the location for EDS spectrum for (g) AW (h) PWHT condition

While coarse grain can be observed near the weld interface of Incoloy 800HT, a very narrower and indistinguishable HAZ was formed owing to its comparatively lower heat conductivity. The microstructure of Incoloy 800HT was found stable and unchanged in the as-welded state. The grains just near to Incoloy 800HT weld interface are classified as HAZ (Figure 4.3(a-b): optical). The presence of carbides in the austenite matrix was deduced from the EDS spectrum shown in Figure 4.3(a). The EDS spectra result for thickened grain boundary with the possibility of grain boundary liquation is shown in Figure 4.3(b) via spectrum at point 2; a high Cr percentage can be inferred to the formation of $M_{23}C_6$ precipitate near grain boundaries. However, the PWHT performed for this study has not shown any effect on the Incoloy 800HT base metal and weld fusion (DuPont, 2009). The presence of Cr, Fe, Al, Ti, and Nb in the alloying composition of Incoloy 800HT contributes to the solid solution hardening. Also, the controlled presence of γ' phase, along with the existence of different carbide phases, contribute to precipitation hardening. The grain size observed in the Incoloy 800HT HAZ was around 180 ± 10 µm.

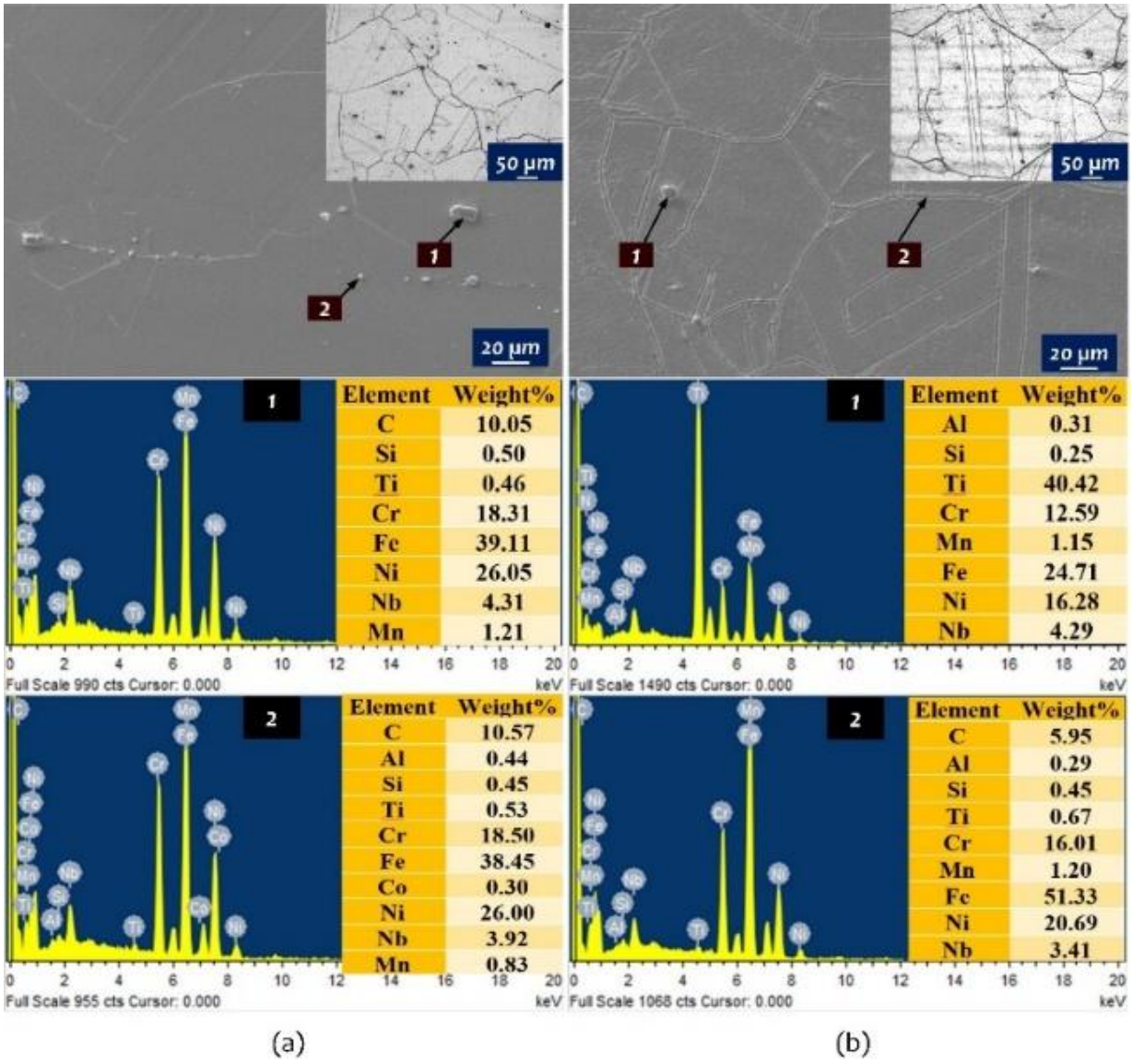


Figure 4.3 : (a) Incoloy 800HT HAZ in AW condition with EDS spectrum for precipitate observed in AW condition (b) Incoloy 800HT HAZ in PWHT condition with EDS spectrum for precipitate observed in PWHT condition

4.1.3 Weld Interface and Fusion Zone (WFZ) Microstructure Characterization

During constitutional supercooling, the solute segregation phenomenon can be observed at the macroscopic level near the weld interface. A noticeable inhomogeneity is present in the chemical composition distribution and microstructure near the weld metal fusion boundary. Every autogenous weld is known to exhibit epitaxial growth, but the nature of dissimilar weld between austenitic metal and martensitic metal leads to the formation of a Type II boundary parallel to the fusion boundary that reduces the possibility of epitaxial growth (Nelson et al., 1998). Figure 4.4(a) clearly illustrates the AW P91 weld interface in which the weld interface, unmixed zone formation, and growth of cells and dendrites can be clearly acknowledged. The presence of macrosegregation can also be established in the form of peninsulas, islands, and beaches. Figure 4.4(b) illustrates the AW Incoloy 800HT weld interface. The illustrated weld interface has a comparatively thicker transition zone (TZ) after the fusion line (Sireesha et al., 2000). It also has a columnar structure, peninsula, and partially mixed zone (PMZ) formation. The difference in melting temperature of employed base metals causes the formation of unmixed zone (UZ) and PMZ. The Incoloy 800HT HAZ has shown thickening of grain boundaries very adjacent to the fusion line, accounting for the precipitation of Ti-enriched particles (Shah Hosseini et al., 2011). Similar results were confirmed in the PWHT state. As presented in Figure 4.4(c), after PWHT P91 weld interface has an unmixed zone and peninsula formation. In Figure 4.4(d), after PWHT Incoloy 800HT weld interface has explicit PMZ formation and HAZ grain boundary

thickening. PWHT does not have any effect on the weld interfaces but only tempers the P91 HAZ martensite.

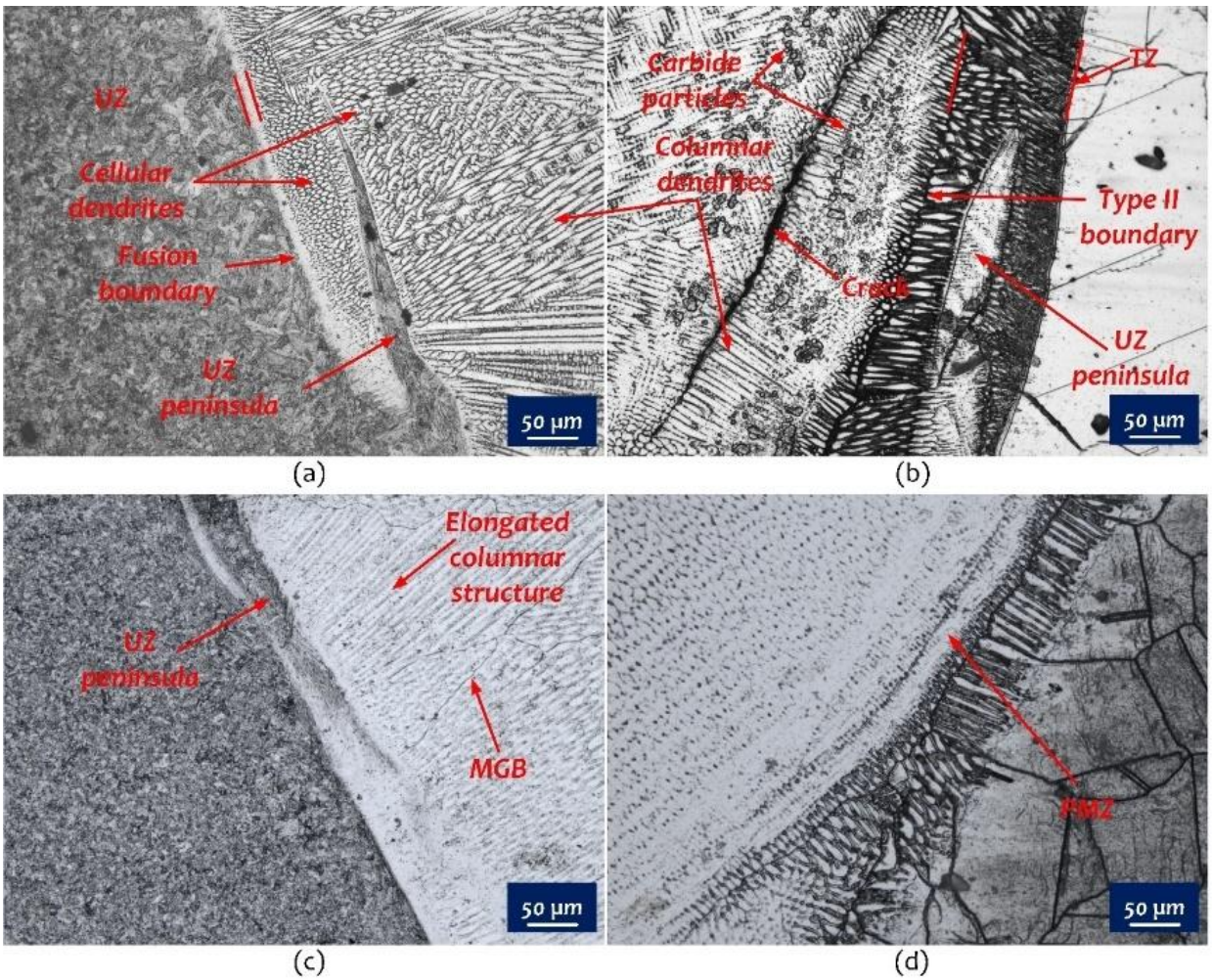


Figure 4.4 : Optical image showing weld interface of (a) AW P91 side (b) AW Incoloy 800HT side (c) PWHT P91 side (d) PWHT Incoloy 800HT side

As weld interfaces are crucial sites for solute segregation to occur, further analysis of elemental distribution across them was done through EDS linear spectra. Figure 4.5(a) shows a decrease in nickel and chromium composition from weld to base metal P91 in AW condition, which corresponds to the P91 composition. A slightly increased Mo concentration in the unmixed zone near the weld interface was observed. A sudden carbon peak suggests the presence of carbide particle precipitate in the weld zone. If noticed corresponding to the carbon peak, there is a Si peak emerging, which could be indicative of M_6C formation. In the Incoloy 800HT interface, as shown in Figure 4.5(b), expected peaks were obtained for Ni, Cr, and Fe as per the metal composition. A sudden increase in appearance in Al could be confirmative regarding the presence of γ' phase. After PWHT, the weld interface of P91 shown in Figure 4.5(c) does not show any significant change in compositional behavior, but a constant distribution of chromium across the weld interface was witnessed. In the PWHT weld interface of Incoloy 800HT (Figure 4.5(d)), all elements confirm the discussed behavior, and no particular change corresponding to PWHT was observed. The dissimilar metal interface microstructure and the UZ features showed minimal changes after PWHT, which might also be due to the austenitic nature of the weld, which limited the microstructural transformations that could occur during the post-weld heat treatment. In Incoloy 800HT HAZ, a rise in V and Ti can be seen at the spotted precipitate.

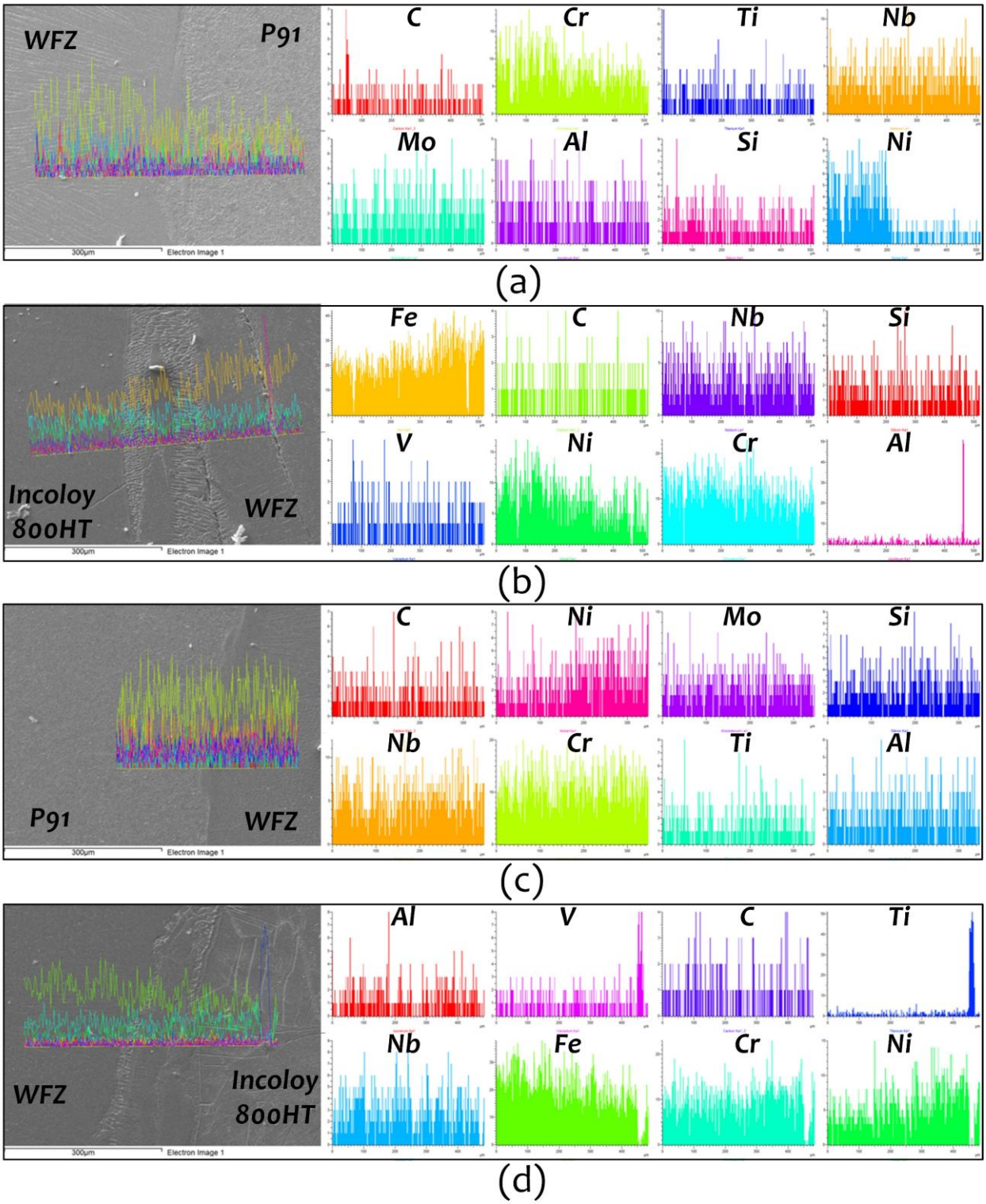


Figure 4.5 : Line map EDS analyses along (a) AW P91 weld interface (b) AW Incoloy 800HT weld interface (c) PWHT P91 weld interface, and (d) PWHT Incoloy 800HT weld interface

The optical images were captured for the entire WFZ for detailed analysis, as shown in Figure 4.6. The different austenitic structures obtained in the austenitic matrix of the WFZ can be categorized on the basis of solidification mode. The solidified microstructure in the WFZ is controlled by the growth rate (R), temperature gradient (G), degree of the constructional supercooling, and alloy composition. The ratio G/R determines the solidification mode, and G*R influences the size of the structure. The growth occurs from unmelted solid grains of base metal; hence, the G/R ratio is higher at the weld interface. The degree of constitutional supercooling affects the temperature gradient, transforming the solidification mode to form cellular, columnar, and equiaxed dendrites. The solidification tends to proceed from the interface to WFZ. Similarly,

different dendritic structures were obtained in the WFZ. It can be perceived from Figure 4.6(a) the formation of different structures overall in the WFZ, the columnar growth was predominated near the base metal interface, and then the solidification mode changes to the cellular and fine cellular structure in the WFZ. Figure 4.6(b) depicts a mixed zone in the WFZ where different dendritic morphologies exist. The different cells or dendrites were separated by a boundary that has a different composition from the bulk WFZ due to solute redistribution known as solidification subgrain boundary (SSGB). The intersection boundary of such a similar group of subgrains or cells can be described as a solidification grain boundary (SGB) (Figure 4.6(c)). At the same time, a high-angle misorientation SGB whose crystallographic component migrates away from its compositional component can be described as a migrated grain boundary (MGB). The dendritic arms and interdendritic cores can also be observed where segregation of alloying elements occurs. Figure 4.6(c) illustrates the solidification cracking phenomenon observed in the WFZ. The crack propagated through the dendrite packet boundaries as uneven solidification in the WFZ induced deformation at the end of solidification. The dominant presence of different cellular structures and unmixed zone 'island' (Figure 4.6(d)) was also spotted near the bottom of WFZ.

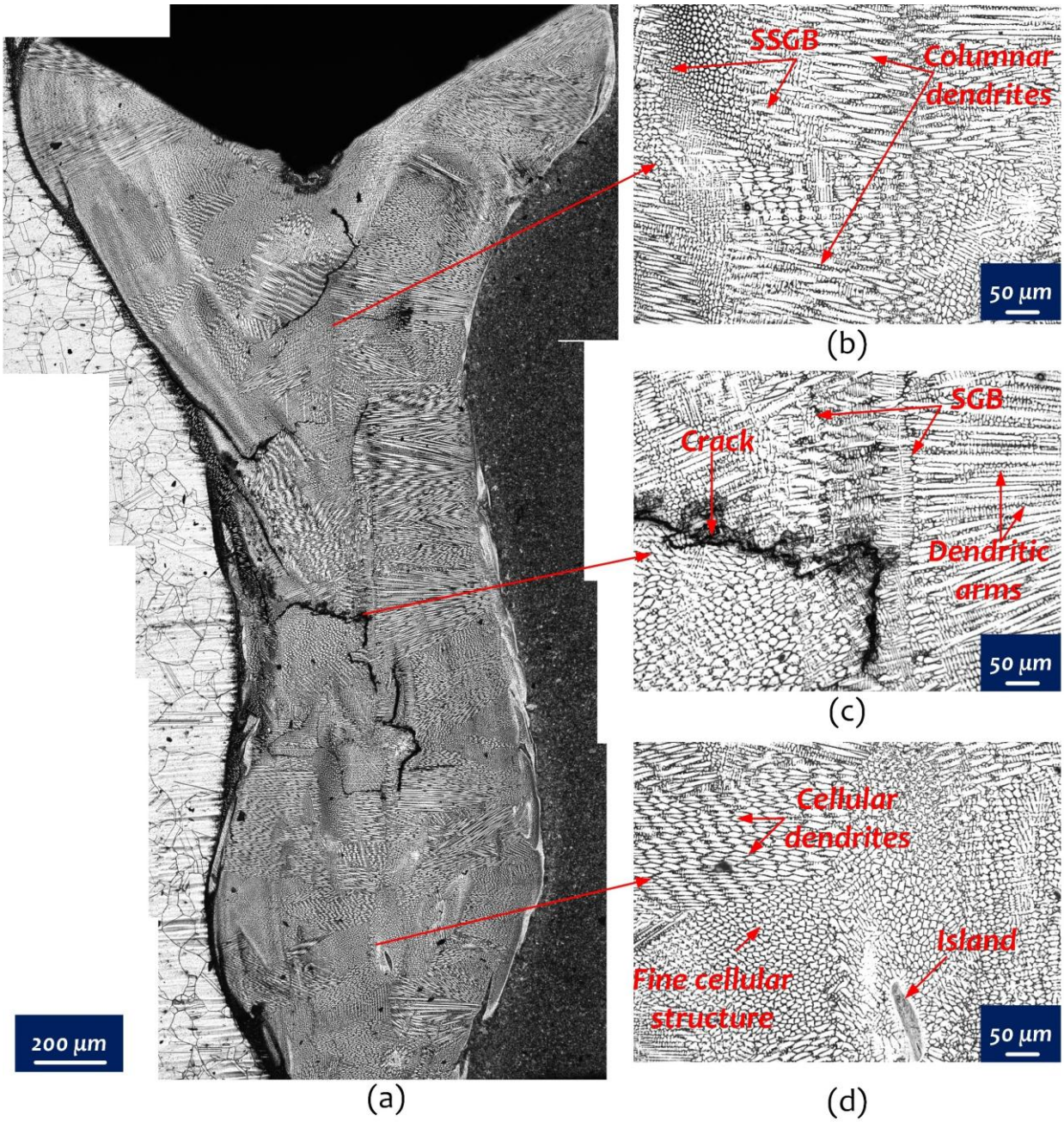


Figure 4.6: Optical images for (a) WFZ in AW condition (b) top WFZ (c) WFZ mixed zone (d) bottom WFZ

Further, the comparative analysis was completed for a PWHT WFZ. However, being austenitic in nature, it did not respond to PWHT. But from a stitched Figure 4.7(a), it can be assumed that cracks were not present along the overall weld length as no sign of cracks were there in the few specimens observed. Figure 4.7(b-d) also confirms the presence of discussed solidification features as the observed top WFZ groups of cellular and columnar structures are indicated with SGB and MGB.

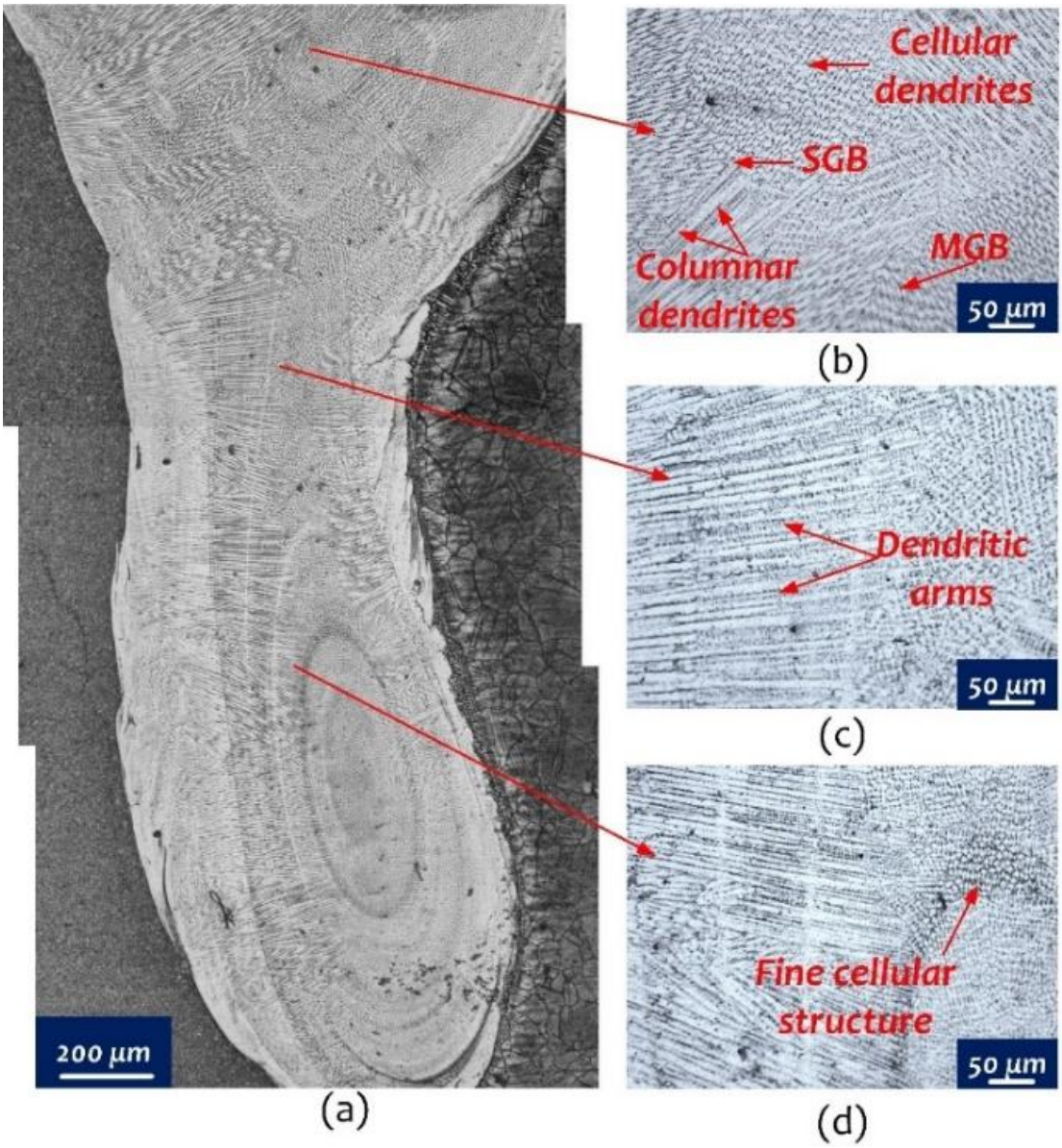


Figure 4.7 : Optical images for (a) WFZ in PWHT condition (b) top of the WFZ (c) WFZ mixed zone (d) bottom

The solidification cracks were observed in the WFZ along the SGBs, as shown in Figure 4.8, the EDS analysis suggests the WFZ phase observed might be a chromium carbide. The cracks were not uniformly distributed along the welded joint. The major cause for this could be the presence of low melting eutectic constituents forming elements, i.e., Nb, Ti, and Si. However, no liquation cracking was observed in the HAZ due to fine and coarse microstructural differences of the base metals. During solidification, the segregation of Nb occurred in the dendritic areas, as shown in Figure 4.9. As the eutectic reaction occurs, the formation of γ/NbC and γ/Laves constituents is reported to take place. Their formation expands the solidification temperature range, leading to uneven cooling and cracking (Radhakrishnan and Thompson, 1991). Nickel has a high affinity for sulfur to form nickel sulfide (NiS) along the grain boundaries and is considered to be the main cause of hot cracking in Incoloy 800HT during welding (Xu et al., 2013). Only Type

1A cracks were observed in the weld region, and no crack formation was witnessed in HAZ regions of either parent metal. More cracks were observed in the weld region near to Incoloy 800HT side interface, which again reflects on the susceptibility of Incoloy 800HT to hot cracking.

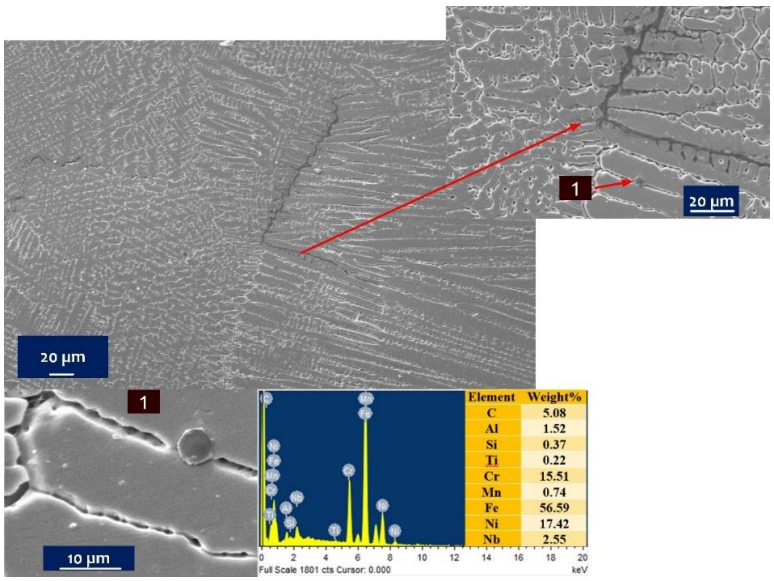


Figure 4.8 : SEM micrograph cracks in AW specimen WFZ and EDS spectra of precipitate observed in the dendritic core region

Figure 4.9 shows the segregation of Mo, Si, and Fe across the dendritic core and subgrain boundaries in the interdendritic region. While the P91 side of WFZ majorly evolved elongated cellular and columnar dendrites. The fusion structures were formed as per the solidification rate, which is affected by the material's physical and chemical properties and also the keyhole mode. Rapid heating and cooling cause the cellular structure to change into dendritic. The keyhole causes a low transfer of heat through the interface to the base metal, which also creates thermally generated stresses. Grain boundaries were found rich in Ti, Si, and Nb concentrations in the weld region. These elements tend to produce complex solidification temperature changes at grain boundaries. Si concentration which was segregated as shown in Figure 4.9, was found in higher concentrations in fusion zone plays a crucial role in hot cracking. As the columnar dendritic structure was observed in the WFZ in large quantity, it is possible that cracks were observed along them, as depicted in Figure 4.8. Carbon affected the formation of a higher columnar dendritic structure which causes partial dissolution of precipitates. Fewer precipitates were observed in the WFZ as Ti consumed C present, and its carbide transferred in the molten pool and accumulated near the Type II boundary.

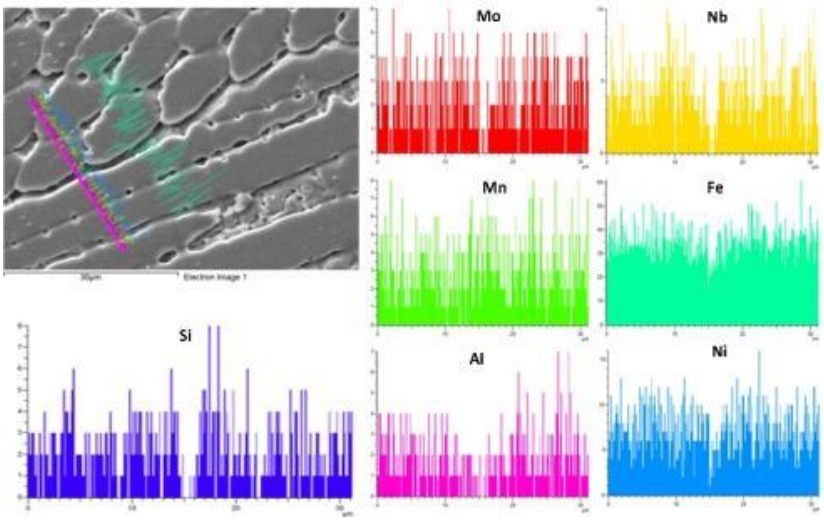


Figure 4.9 : Line map EDS analysis across the interdendritic cores in the weld region

4.1.4 Tensile Properties

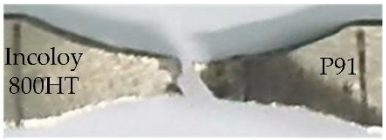
The tensile tests were conducted on the transverse tensile specimen, and the test results are mentioned in Table 4.1. The trend of stress and strain can be observed and compared through engineering stress-strain obtained, as shown in Figure 4.10(a). The tensile strength of the AW joint (standard specimen) was measured at 546 ± 6 MPa, which was lower than the tensile strength of both the base metal P91 (687 ± 8 MPa) and Incoloy 800HT (593 ± 5 MPa). In AW condition, the fracture was observed in the region of the Incoloy 800HT HAZ, as shown in Table 4.2. After the PWHT, fracture occurred in the region of Incoloy 800 HT base metal with a tensile strength of 576 ± 5 MPa, which was still lower than the P91 and Incoloy 800 HT base metal. However, fracture from the region of the Incoloy 800 HT base metal ensures that the joint is safe for USC boiler service after the PWHT. The yield strength of the welded joint was measured at 265 ± 4 MPa and 297 ± 5 MPa for the AW and PWHT joint, which was close to the yield strength value of the Incoloy 800 HT base metal (285 ± 4 MPa). Base metals exhibited the highest tensile and yield strength (YS), while the welded specimens have shown resembling results reported in another study (Vellaichamy et al., 2018). For the sub-size specimen, the fracture was observed in the center region of the WFZ, and strength was measured at 565 ± 5 MPa and 549 ± 4 MPa for AW and PWHT conditions, respectively. The failure from the center region of the WFZ might be due to the presence of the solidification cracks, which showed the sudden propagation just after the yielding. However, the presence of segregation-induced brittle phases near the fusion boundaries may act as initiation points for premature failure under tensile loading. Still, with lower yield strength observed in AW and PWHT conditions, tensile strength was obtained in the reported range.

The fractured tensile specimen was also analyzed using the FESEM and presented in Figure 4.10(b-e). The presence of the dimples at the fracture surface also supports the results (% elongation) obtained through the tensile tests. Figure 4.13(b-c) shows that a ductile mode of fracture occurs in standard-size specimens failing from Incoloy 800HT HAZ (AW) and base metal (PWHT) as dimples were uniformly distributed. The fracture specimens in AW and PWHT conditions exhibit ductile dimples of varying size and depth, microvoids of varying size and depth, and tear ridges. The PWHT fractured specimen also shows the presence of a few brittle areas, i.e., cleavage facets (Figure 4.10(c)). While sub-size AW and PWHT specimens failing from weld had gone through the intergranular and transgranular type of fracture, fewer dimples suggest slight ductile behavior (Figure 4.10(d-e)). The appearance of the fracture surface also supports the tensile test results. The fracture surface for the AW specimen exhibits a large area of the cleavage facets (Figure 4.10(d), while after the PWHT, both fine dimples and microvoids were observed along with the cleavage facets (Figure 4.10(e). The cracks were dominated in the weld bead due to instability caused by the initiation of the keyhole and high heat input, or the liquid metal may have filled the cracks to heal them slightly, as represented in Figure 4.6(c). Figure 4.11(a-d) depicts the crack along with the columnar dendritic microstructure and the re-solidification in the crack (Nelson et al., 1998). The % elongation measured for sub-size specimens were 198 ± 3 MPa and 206 ± 4 MPa, respectively for AW and PWHT, respectively, which was lower than the corresponding values of a standard tensile specimen. The % elongation was also measured lower than the standard tensile specimen, and it was 22 ± 2% and 15 ± 2% for AW and PWHT joint.

Table 4.1 : Tensile test results

Specimens	*UTS (MPa)*	*YS [offset 0.2%] (MPa)*	*Elongation (%)*	*Reduction in area (%)*
AW (Standard specimen)	546 ± 6	265 ± 4	25 ± 2	48 ± 4
AW (Subsize specimen)	565 ± 5	198 ±3	22 ± 2	48 ± 5
PWHT (Standard specimen)	576 ± 5	297 ± 5	27 ± 3	53 ± 3
PWHT (Subsize specimen)	549 ± 4	206 ± 4	15 ± 2	40 ± 4

Table 4.2 : Fracture locations for the tensile tested specimen in different conditions

Specimen	*AW*	*PWHT*
Standard	 From Incoloy 800HT HAZ	 From Base Metal
Sub-size	 From WFZ	 From WFZ

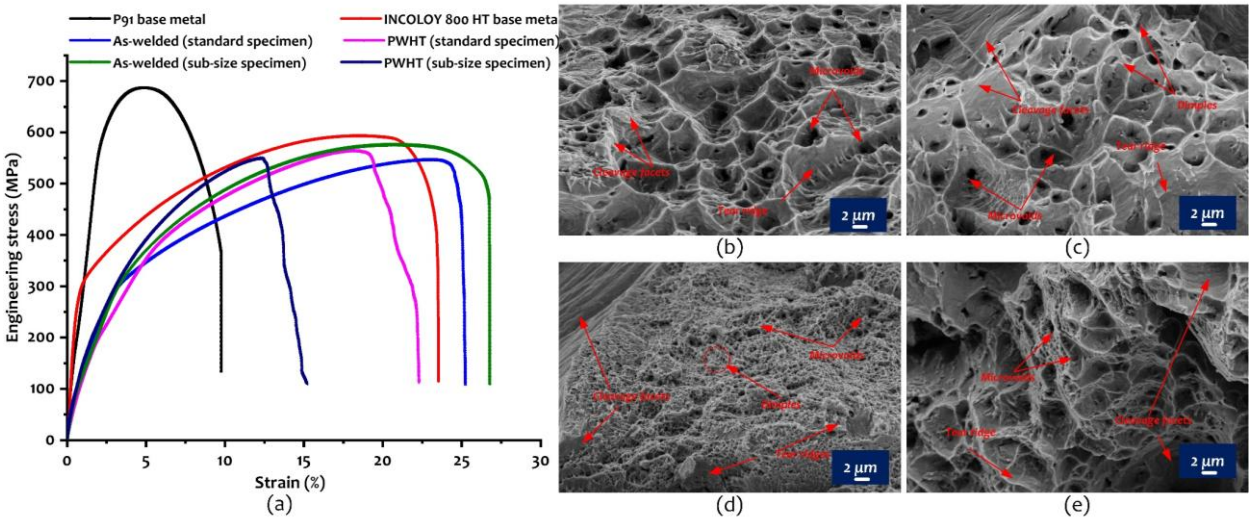


Figure 4.10 : (a) Engineering stress-strain curves for performed tensile tests; SEM fractography micrographs of (b) standard AW specimen, (c) standard PWHT specimen, (d) sub-size AW specimen, (e) sub-size PWHT specimen

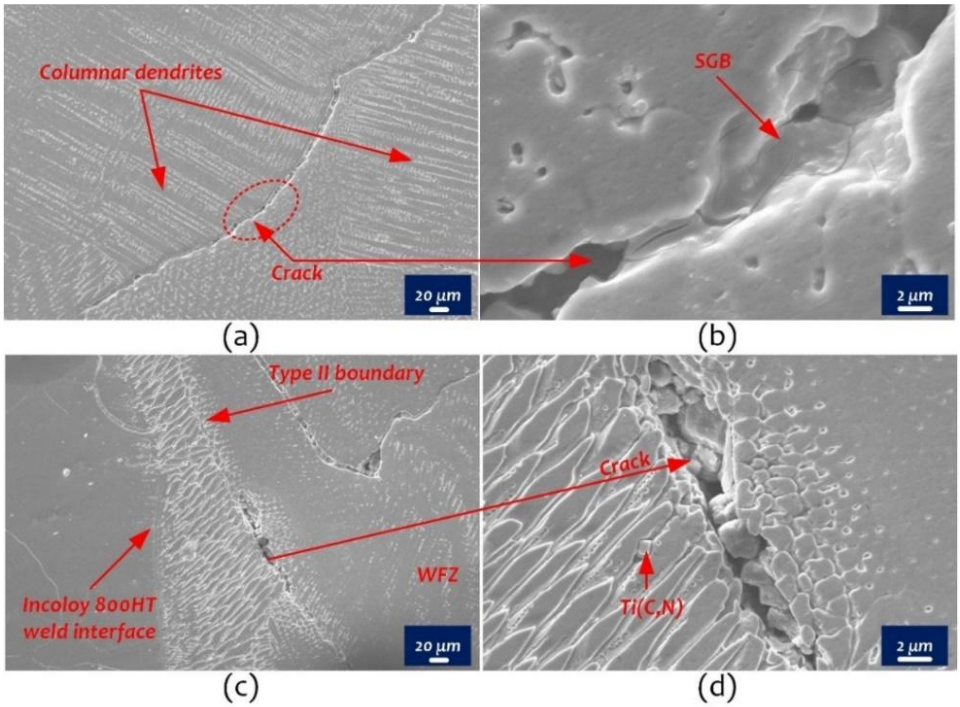


Figure 4.11 : SEM micrograph for PWHT specimen (a) WFZ, (b) crack along SGB, (c) PWHT Incoloy 800HT weld interface, (d) crack along Type II fusion boundary

4.1.5 Microhardness Properties

The inhomogeneity in microstructure obtained due to the welding of dissimilar metals impacts the mechanical property of the weld joint. Hence, microhardness analysis was conducted for the categorized welding zones. The comparison was done in AW and PWHT states, as illustrated in Figure 4.12. The obtained microhardness for the base P91 and Incoloy 800HT was 245 ± 5 HV and 189 ± 5 HV, respectively. A comparatively lower hardness of 187 ± 3 HV) was observed in the weld fusion zone of the AW joint, which was attributed to the austenitic microstructure and segregation of the alloying elements at the interdendritic boundaries. A uniform hardness variation was measured in the WFZ except for the Incoloy 800HT, which showed a slight increase in hardness that could be attributed to the formation of the unmixed zone due to differences in melting temperatures of parent base metals. The illustration shows a notable variation in the measured hardness along the weldment. The AW P91 side HAZ showed a significant increment in hardness with a peak hardness of 391 HV near the weld interface, i.e., CGHAZ. P91 CGHAZ, being martensitic in nature, showed higher hardness due to the presence of a slightly higher alloying concentration of Mo, W, C, and N. The complete dissolution of MX and $M_{23}C_6$ precipitates in the region P91 CGHAZ formed under high temperature (>>A_{c3}) increases the percentage of carbon and nitrogen in the solution matrix, hence causing the increase in hardness by solid solution strengthening. A similar observation has also been reported for P91 CGHAZ (Pandey and Mahapatra, 2016; Wang et al., 2016). However, the hardness of P91 CGHAZ in the fusion welded joint was reported much higher than the laser beam welded joint (Abd El-Rahman Abd El-Salam et al., 2013; Kulkarni et al., 2019a; Pandey et al., 2019b). Gradually, a lower hardness in P91 FGHAZ was observed, varying from 387 HV to 356 HV with an average of 373 ± 12. The incomplete dissolution of precipitates in FGHAZ as a result of lower peak temperature (≥A_{c3}) might be the cause of the poor hardness in P91 FGHAZ than in the P91 CGHAZ. The minimum hardness in P91 HAZ was measured in ICHAZ, which experienced the temperature between A_{c1} and A_{c3}. The poor hardness of 218 HV in P91 ICHAZ was attributed to the re-tempering of martensite, grain, and precipitate coarsening. In the AW condition, the carbide and nitride precipitates imparted the hardness to Incoloy 800HT, but being austenitic in nature, it exhibited comparatively lower hardness than P91 and did not show any significant variation. Owing to this property of Incoloy 800HT, the HAZ hardness was measured at 195 HV, closely comparable to the Incoloy 800HT base metal hardness.

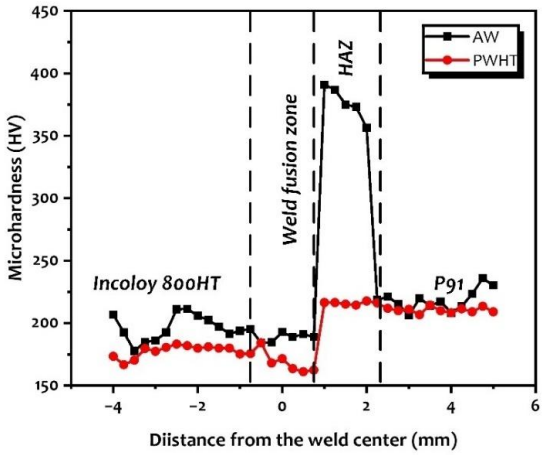


Figure 4.12 : Microhardness variation obtained for AW and PWHT weldments

The tempering of the welded joint showed a significant effect on the hardness value of the P91 HAZ, while the hardness of the WFZ and Incoloy 800HT HAZ remained unaffected. After PWHT, a lowering in the hardness of P91 HAZ was significant due to the tempering of martensite. The dissolved precipitates in AW condition were resurfaced while tempering. Hence, the CGHAZ of P91 after PWHT depicted a sharp decline of 174 HV in hardness compared to the AW state. A drastic reduction in hardness of the P91 FGHAZ was also measured, and it was 356 HV. However, the hardness of the P91 ICHAZ remains unaffected, and it was 218 HV. A similar trend of the hardness variation in P91 HAZ was also reported by (Pandey et al., 2017). While theoretically, austenitic Incoloy 800HT and WFZ do not respond to PWHT, but slight reduction

can be observed in the Incoloy 800HT side and even in the WFZ. This might be due to softening by carbide dissolution (Nelson et al., 1998). Also, aging might be argued for this reduction in hardness (Sireesha et al., 2000). PWHT can be concluded to be successful in reducing the hardness in the martensitic HAZ as well as the reduction in hardness variation along the weldment.

4.1.6 Charpy Impact Toughness

The energy absorbing capacity of the welded joint was evaluated by performing the Charpy impact toughness test at room temperature, and the results are shown in Table 4.3. The fractured impact tested specimen is shown in Figure 4.13(a-b). The Charpy impact toughness of the WFZ was measured at 65 ± 4 J in AW condition, which was very low as compared to the Charpy impact toughness of the P91 base metal (105 ± 4 J) and Incoloy 800 HT base metal (102 ± 5 J). The poor impact toughness value for the WFZ was attributed to the presence of solidification cracks along the SGBs and MGBs in the weld and the segregation of the alloying elements along with the interdendritic areas. However, it met the EN ISO 15653:2018 standards' recommended minimum Charpy impact toughness of 47 J (The British Standards Institution, 2018). In addition, the Boilers and Pressure Vessel Code published by the American Society of Mechanical Engineers (ASME) specifies a minimum Charpy impact toughness value of 41 J as a requirement for qualifying (ASME Section VIII Division 1, 2019). The fractured impact specimen showed the complete fracture of the specimen into two parts for both AW and PWHT joints. In DWJ, the results showed the maximum Charpy impact toughness for the P91 base metal compared to the WFZ and Incoloy 800 HT base metal. The Charpy impact toughness in the WFZ after PWHT was measured at 55 ± 2 J. The increase in Charpy impact toughness of the WM after the PWHT was also reported in the previous study (Thakare et al., 2019). As illustrated in Figure 4.14(a-b), the fractography analysis shows the formation of narrow and deep dimples, which confirms the ductile mode of failure mixed with intragranular fracture. It seems complicated to comment on the loss of ductility. It could be either due to the presence of solidification cracks or due to the formation of secondary carbides.



Figure 4.13 : Samples fractured under Charpy impact testing from (a) WFZ (b) HAZ P91 (c) HAZ Incoloy 800HT (d) PWHT WFZ (e) PWHT HAZ P91 (f) PWHT Incoloy HAZ

Table 4.3 : Charpy Impact toughness obtained in Charpy impact toughness testing

Specimens	*Impact Zone*	*Charpy impact toughness (J)*
AW	WFZ	65 ± 4
PWHT	WFZ	55 ± 2

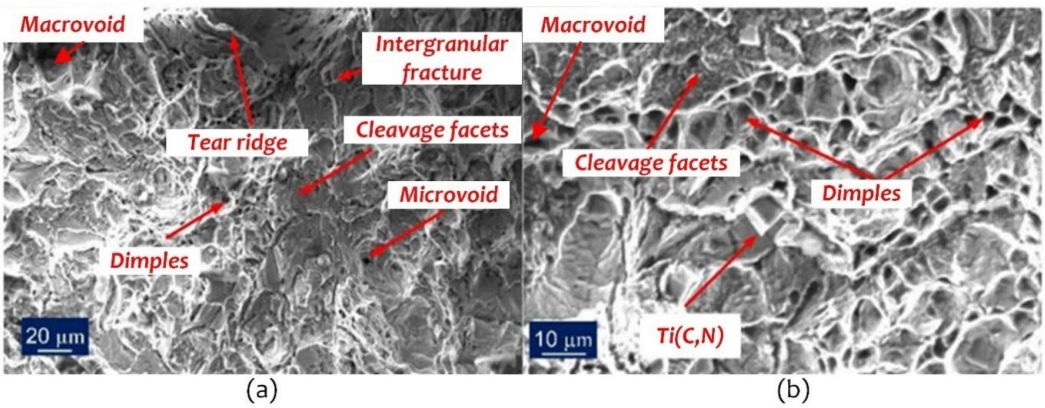


Figure 4.14 : SEM fractography micrograph of specimens broken during Charpy impact toughness test (a) AW (impact at WFZ), (b) PWHT (impact at WFZ)

4.2 ELECTRON BEAM WELDING (EBW)

4.2.1 Macroscopic Observations

The welded plate is shown in Figure 4.15(a). From the macroscopic observation, a clean weld bead was witnessed, and there was slight depression at the weld's start due to the dwell time. The weld root showed no presence of suck-back concavity, cracking, undercut, or lack of penetration. The observed cross-sectional macrostructure showed that the weld root face had complete and continuous penetration. The single-pass electron beam deposition in EBW did not produce any distortion in the welded plates. The cross-section of the welded joint was observed to witness the weld bead and depth of penetration, as shown in Figure 4.15(b). Throughout, complete penetration was observed up to 8 mm. The macrostructure revealed the narrower weld bead. This shape of the weld bead is due to the keyhole mode of EBW, offering a high depth-to-width ratio. The P91 HAZ is visible in the macrostructure, and its thickness varied from the top of the weld and decreased slightly up to the weld root. This gradual variation in HAZ is dependent on the temperature variation. The temperature was higher at the weld face than at the weld root. Hence HAZ region near the top region of the weld is significantly wider. The HAZ region width was measured to be around 1 mm and less. The width of the weld bead in the center was around 1.9 mm.

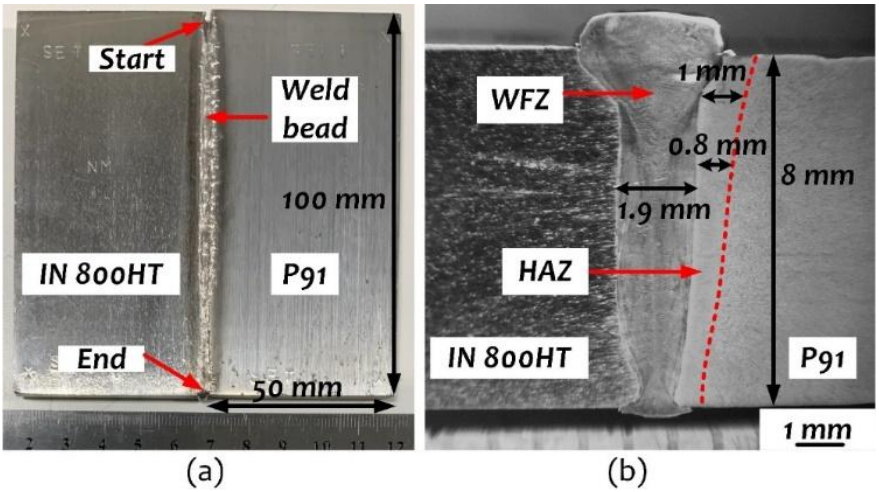


Figure 4.15: (a) Electron beam welded plate in AW state (b) macrostructure of weld seam in AW state

4.2.2 Weld Interface and Weld Fusion Zone (WFZ) Microstructure Characterization

EBW offers low heat input, leading to a narrower HAZ region. Figure 4.16(a) shows a stitched view P91-Incoloy 800HT welded joint under an optical microscope. The WFZ clearly shows the austenitic solidification mode due to the melting of Incoloy 800HT primarily. Since heat input is low, its effects are not adverse in the HAZ. The P91 HAZ region is characterized into three different regions, as described in Figure 4.16(a), namely CGHAZ, FGHAZ, and ICHAZ. The Incoloy 800HT HAZ region did not show any increase in grain size, as austenite is quite a stable microstructure at high temperatures. Figure 4.16(a) gives a good view of the weld fusion zone, where it was seen that the solidification converges right at the center, and a precise formation of the centerline was observed. Also, a V-shaped conical arrangement in the top region of WFZ was witnessed due to the nature of the striking electron beam, and the concerned region must be the last to solidify. Further, an EDS line scan mapping (Figure 4.16(b)) confirmed that WFZ contained a composition similar to Incoloy 800HT. Figure 4.16(c) shows that the presence of Cr and Nb was in similar amounts on the Incoloy 800HT side and WFZ. A sudden decrease was observed on the P91 side since P91 has comparatively lower percentages of Cr and Nb. Fe variation was slightly higher in the WFZ. The HAZ did not need any detailed characterization as no significant changes were observed in the zones, and they were similar to the zones, as discussed in section 4.1.2.

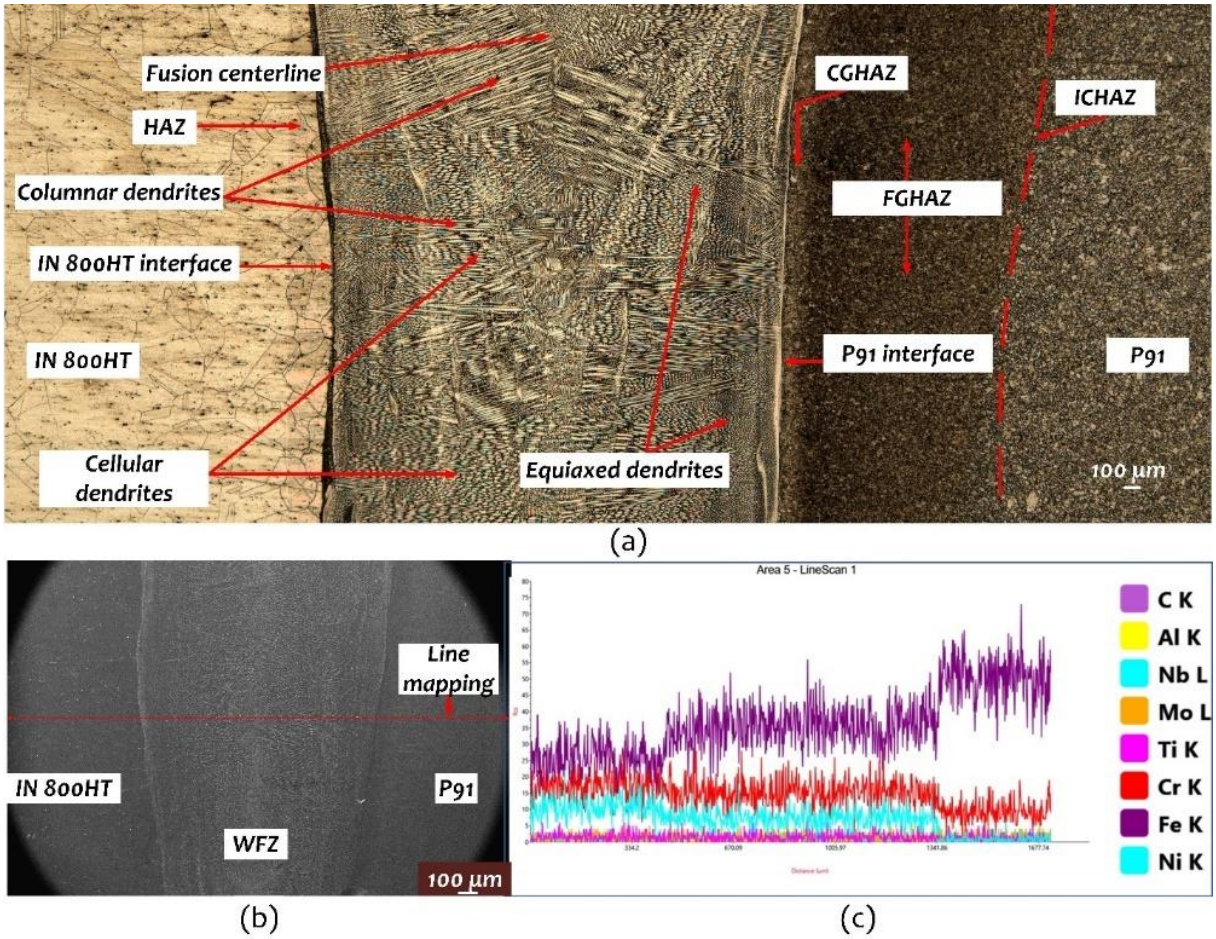


Figure 4.16: (a) Stitched optical micrographs of electron beam weld (b-c) EDS line map spectrum across the weld bead

The WFZ and weld interfaces were observed under an optical microscope. The optical images in Figure 4.17(a-i) were taken from the AW state specimen, while images in Figure 4.17(j-l) were taken from the PWHT state specimen. Figure 4.17(a,b,c) shows the P91 weld interface, WFZ, and Incoloy 800HT weld interface from the weld top region, respectively. Figure 4.17(d,e,f) shows the P91 weld interface, WFZ, and Incoloy 800HT weld interface from the weld center region, respectively. Figure 4.17(g,h,i) shows the P91 weld interface, WFZ, and Incoloy 800HT weld interface from the weld root region, respectively. Optical investigations performed on the P91 weld interface indicated the presence of macrosegregation in the form of peninsulas and an unmixed zone (UZ) running parallel to the weld interface. The UZ formation was very limited, and macrosegregation was not particularly severe either. The Incoloy 800HT weld interface was relatively thicker, with the formation of the transition zone (TZ) and Type II boundary. Type II boundaries are associated with in-service cracking and disbanding. WFZ had all the features confirming the occurrence of the keyhole phenomenon. WFZ in the top region was observed with a separately solidified V-shaped conical section, which indicates the region where the electron beam strikes and the region must have solidified at the last. The WFZ center region was observed with the centerline where solidification occurred near the end and had an extensive columnar-type dendritic structure. The WFZ near the weld root also had the fusion centerline, but the region was heavily distributed with equiaxed and cellular-type dendritic structures. Overall, the WFZ was randomly distributed with cellular and equiaxed type dendritic patches, while columnar type dendritic growth was dominant in the weld center region. The presence of cuboidal precipitates Ti(C,N) was also witnessed. Several types of grain boundaries, including solidified grain boundaries (SGBs), solidified subgrain boundaries (SSGBs), and migrating grain borders (MGBs), were seen in the WFZ. SGBs and SSGBs are formed as the liquid film between two grains and dendrites solidify at last, respectively. The MGB formation was less in WFZ as rapid solidification of WFZ restricts the movement of the crystallographic component of SGB from its compositional component.

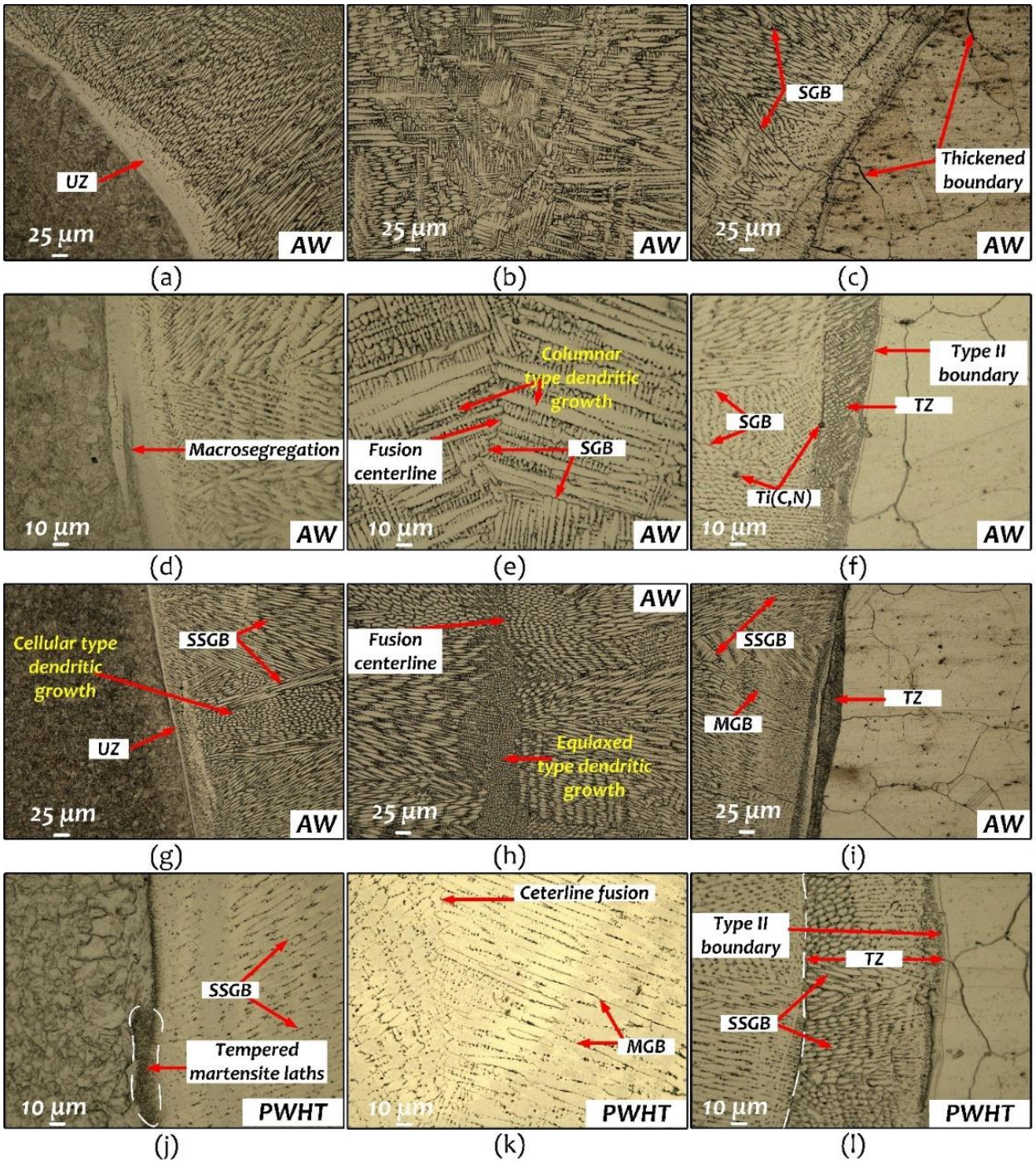


Figure 4.17 : Optical micrographs of (a) P91 weld interface (near weld top) (b) WFZ (near weld top) (c) Incoloy 800HT weld interface (near weld top) (d) P91 weld interface (near weld center) (e) WFZ (near weld center) (f) Incoloy 800HT weld interface (near weld center) (g) P91 weld interface (near weld root) (h) WFZ (near weld root) (i) Incoloy 800HT weld interface (near weld root) (j) P91 weld interface (near weld center) (k) WFZ (near weld center) (l) Incoloy 800HT weld interface (near weld center)

Figure 4.17(j,k,l) displays the P91 weld interface, the WFZ weld interface, and the Incoloy 800HT weld interface, respectively, from the weld center region in the PWHT condition. There was no discernible change in the microstructure of the weld interfaces or the WFZ due to the PWHT. However, in the PWHT specimen, the presence of tempered martensite was witnessed near the P91 weld interface. It suggested that P91 melt was limited near the interface and could not be thoroughly mixed in the WFZ. In addition, an EPMA analysis was carried out in order to investigate the diffusion and segregation that occurred at the weld interfaces as well as the regions that were close by in the solidified WFZ. Figure 4.18 illustrates the qualitative area mapping results that were obtained from the EPMA investigation of the P91 weld interface. The

development of various carbides (Mo, Ti, and Cr-based) must be to blame for the enrichment of carbon in the WFZ that was located close to the P91 weld interface. Nb was present in lower percentages, and its distribution across the weld interface was homogenous, with no hint of segregation into dendritic growth at the weld interface. Cr was higher in WFZ since WFZ was mainly formed from Incoloy 800HT melt and Ni. On the P91 side, there was a larger concentration of Fe, and there was a modest hint of diffusion along the weld interface. Figure 4.19 displays the EPMA results for the Incoloy 800HT weld interface now. There was evidence of significant carbide (C-rich) precipitates in the transition zone (TZ) that developed close to the weld interface. On closer inspection, it was discovered that the Ti-rich precipitates were evenly dispersed across the whole Incoloy 800HT weld interface. The Cr% was found to be lower in the WFZ region that was close to the Incoloy 800HT weld interface. This could be due to the movement of Cr in the interdendritic regions, but segregation was not visible in the results. Fe cannot segregate, so the comparatively higher Fe concentration in WFZ can only be reasoned by diffusion activity. Ni diffusion was prominent near the TZ since this region solidifies at higher rates, and the alloying elements are accumulated at the grain boundaries. Mo was found well distributed in the WFZ. The EPMA scans were unable to confirm its segregation due to the low resolution of the scan or potentially due to the increased cooling rate of WFZ near the weld interface, which may have hindered its movements. However, it is possible that both of these factors contributed to the inability to confirm its segregation. The EBSD scan (Figure 4.20) showed random orientation of the P91 HAZ grain near the P91 weld interface in the WFZ. The IPF map showed different orientations of the dendritic groups in the WFZ. The KAM map indicated high levels of local strains in the P91 HAZ and uneven distribution in the WFZ, which could contribute to failure under tensile loading.

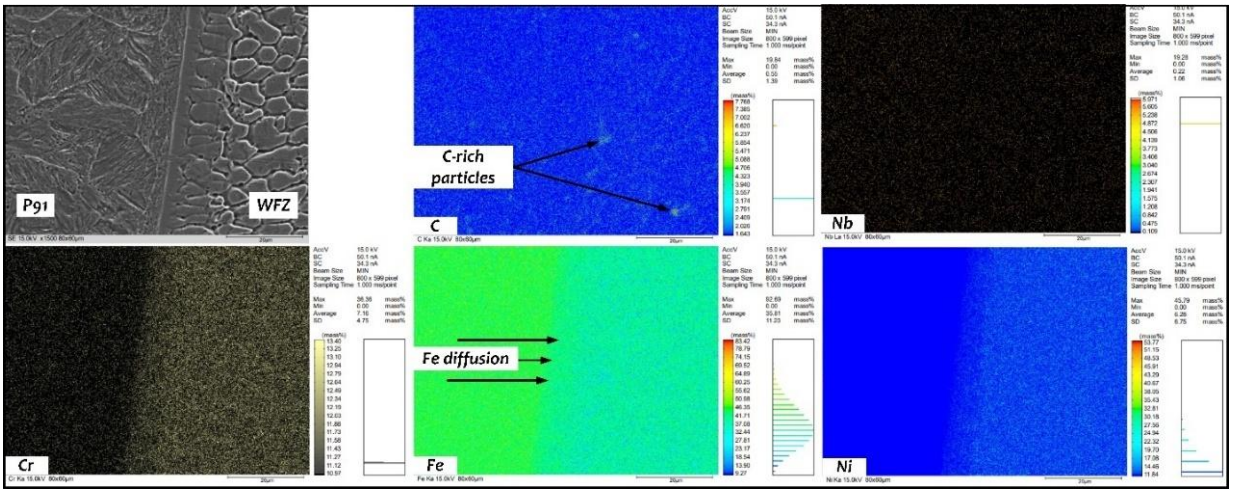


Figure 4.18 : EPMA qualitative analysis of P91 weld interface

The EBSD scan at the Incoloy 800HT weld interfaces is shown in Figure 4.21. The EBSD results not only confirm the previously mentioned observations but also bring out some additional information. Figure 4.20(a) and Figure 4.21(a) demonstrated that there was evidence of dendritic growth at the weld interfaces of P91 and Incoloy 800HT near the WFZ. The orientation of the grains in the WFZ is completely different from that of the base metal in the instance of the P91 weld interface. On the other hand, epitaxial grain development was noticed in the Incoloy 800HT interface, and it had an essentially identical orientation (Figure 4.21(a)) on either side of the fusion line. The epitaxial grain growth could occur in dissimilar welding if the BM and WFZ have similar crystal structures and compositions. However, the grain size near the Incoloy 800HT interface was quite small, suggesting very quick solidification near the weld interface.

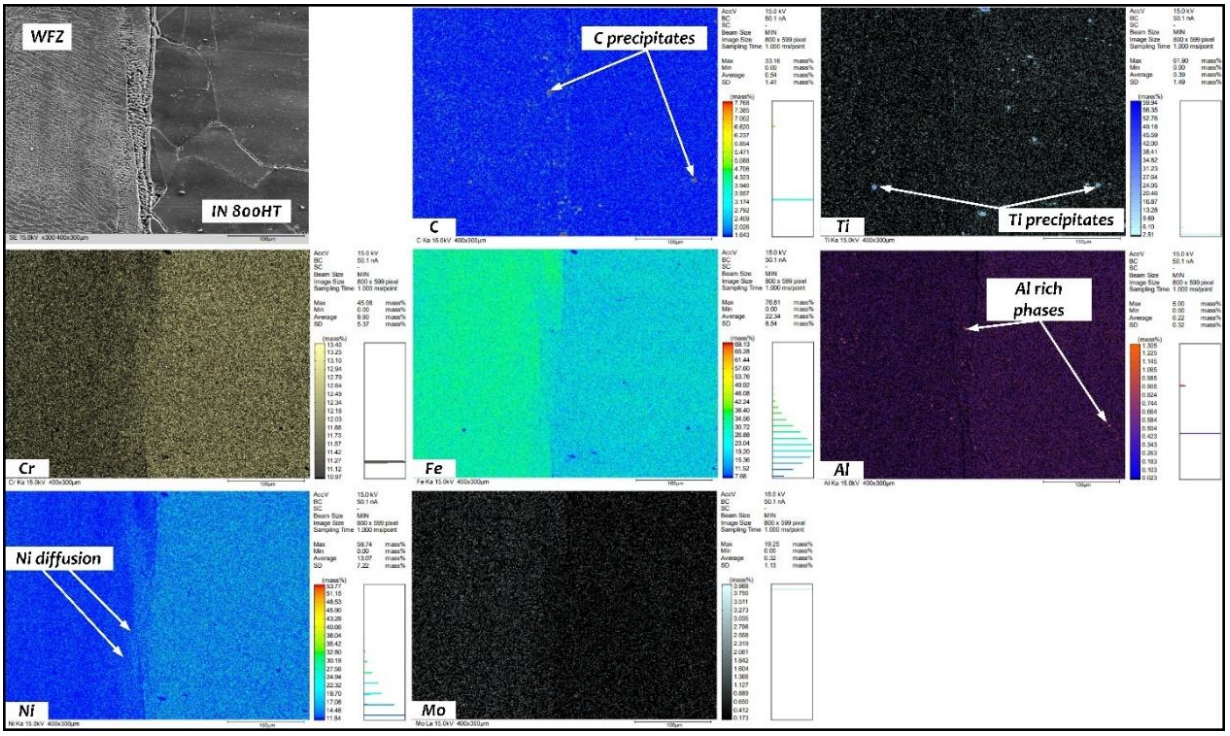


Figure 4.19 : EPMA qualitative analysis of Incoloy 800HT weld interface

The Kernel average misorientation (KAM) map (Figure 4.20(b)) indicated high levels of local strains in the P91 HAZ and uneven distribution in the WFZ. The KAM map revealed higher dislocations and strains near the weld interface compared to the HAZ regions. The phase maps indicated the presence of BCC orientation (Figure 4.20(c)) in the P91 HAZ and near the P91 weld interface. FCC orientation (Figure 4.21(c)) was in the Incoloy 800HT and WFZ. WFZ consisted of FCC structures mainly. It could be inferred from the results that WFZ solidification was austenitic (Fei et al., 2020). The KAM map showed an uneven distribution of dislocations across the weld interface, which makes the WFZ and HAZ regions prone to failure. In a similar study by (Sakthivel et al., 2022), in the P91 HAZ region, KAM displayed a greater strain distribution, which was a contributing factor to the failure. In the present study, the quality of scans was not optimal, as significant noise was present in the WFZ. This was because the samples were manually polished, and the step size was 0.1 μm. In summary, the EBSD scan on the P91 and Incoloy 800HT weld interfaces confirmed misorientations and the presence of different phases.

The results from EBSD analyses do not lie in agreement with the fact that Incoloy 800HT was the weakest link, as the failure occurred from the base metal. The KAM map (Figure 4.21(b)) showed high strain distribution in the P91 HAZ; hence, failure must have occurred from the P91 HAZ region. The microstructure of a material, which includes the grain size, grain shape, grain boundary orientation, and other characteristics, is one of the most important determinants of the tensile strength of that material. The KAM map provides information on the degree of crystallographic misorientation between neighboring grains, which can be an indicator of the grain boundary character. Materials with low KAM values tend to have stronger tensile strength, as the grain boundaries are more coherent and less likely to initiate cracks.

On the other hand, materials with high KAM values may have weaker tensile strength, as the grain boundaries are more likely to be sites of initiation for cracks and other defects. It is important to note that tensile strength is a complex property that depends on many factors, and the relationship between KAM and tensile strength is not always straightforward. There are exceptions to the general relationship between Kernel Average Misorientation (KAM) and tensile strength. In some cases, high KAM values can lead to improved tensile strength due to the presence of substructures, such as secondary phase particles, that reinforce the material and enhance its mechanical properties. Additionally, other factors, such as the type of loading, the

presence of defects or inclusions, and the material's processing history, can significantly impact the tensile strength and overwhelm the effect of KAM. In support of such exceptional behavior, the notable work of (H. Zhang et al., 2021; Zhou et al., 2020) reports that failure in Ni-based superalloys occurred in the region of the EBSD KAM map displaying the highest measured concentration of stress.

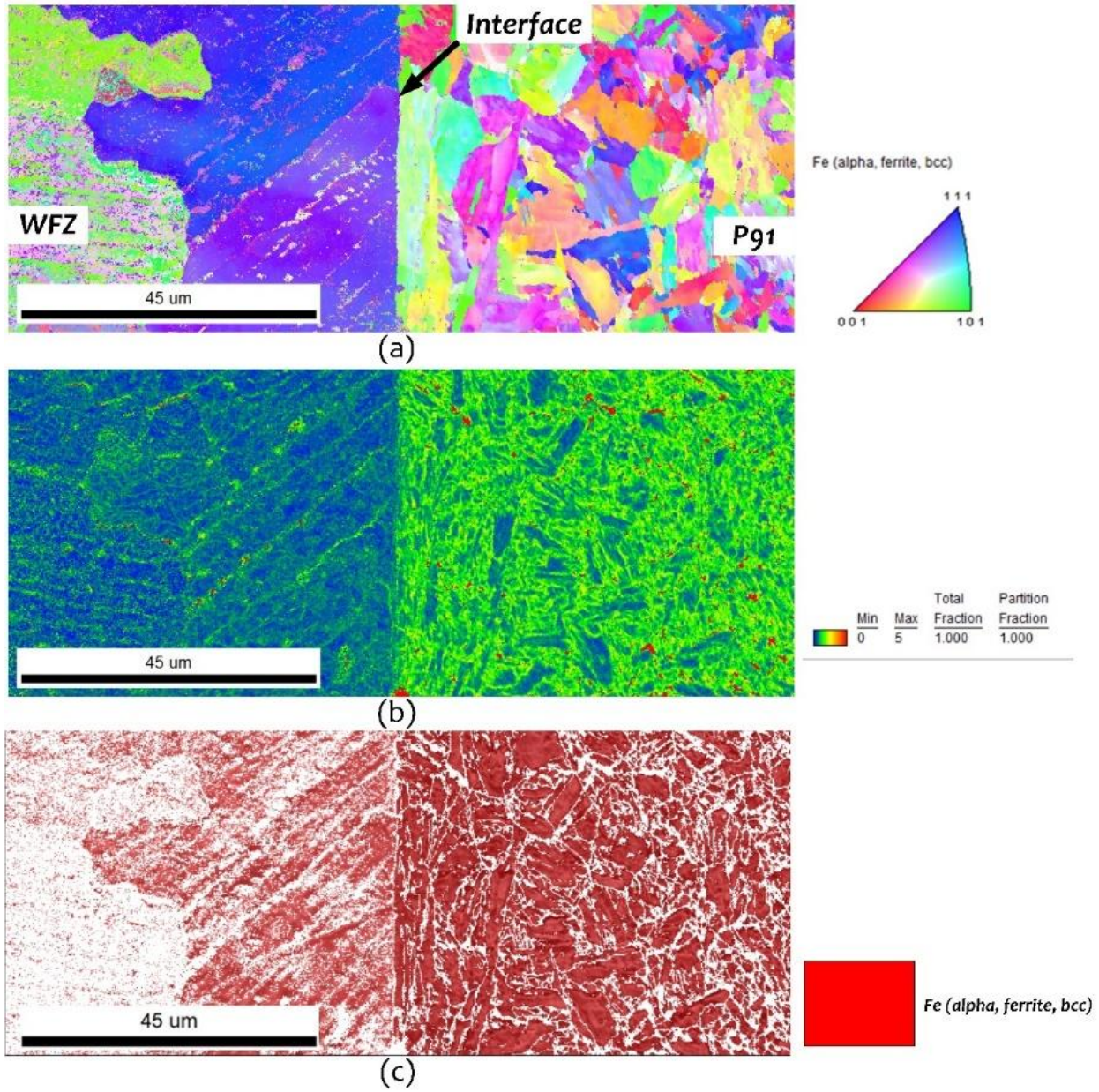


Figure 4.20 : EBSD scan at P91 weld interface : (a) IPF map (b) KAM map (c) phase map

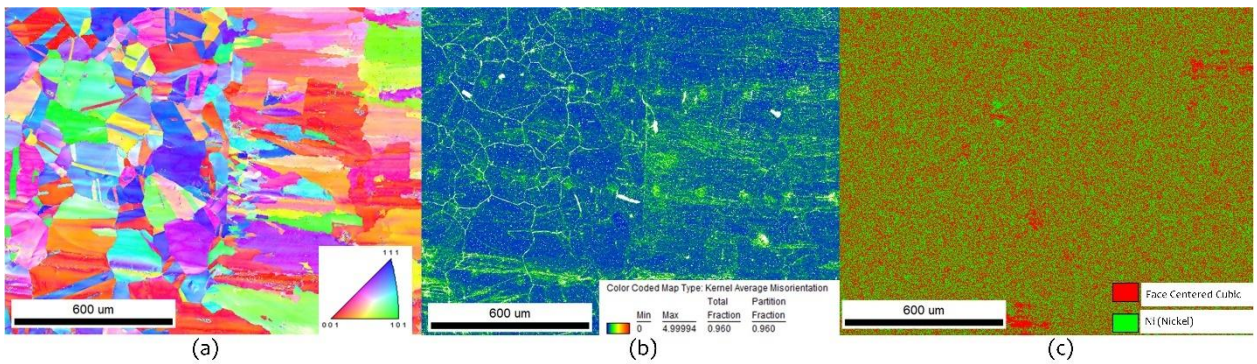


Figure 4.21 : EBSD scan at Incoloy 800HT weld interface : (a) IPF map (b) KAM map (c) phase map

Figure 4.22(a-b) shows the WFZ in AW and PWHT states. The cellular-type dendritic regions in AW and PWHT states can be seen in Figure 4.22(c-d), with SSGBs, SGB, interdendritic particles, and dendritic cores. The EDS spectrum of the interdendritic particles in Figure 24(e) shows Ti, Mn, and Cr-based particles. Further, an EDS area map (Figure 4.22(f)) shows the presence of TiN precipitate in the WFZ. In interdendritic regions, the Ti is diffused into a liquid phase, while solidification results in the formation of finer Ti(C, N) precipitates (Tan et al., 2011). During the EBW process, the WFZ regions are exposed to different cooling rates, and from weld seam observation, a varied distribution of dendrites was witnessed. EBW process is preferred because it provides low heat input and rapid solidification. It contributes to the reduction of the amount of segregation that occurs as a result. By interpreting the partition coefficient, which is also known as the segregation coefficient k, one is able to make an estimate of the extent to which the alloying elements segregate (Xing et al., 2014). The segregation coefficient was calculated by taking the ratio of element concentration obtained through EDS and EPMA. The ratio was determined based on the average element concentration of the alloying elements found in the dendritic core (solid phase) and interdendritic region (liquid phase) of the WFZ. If k tends to be greater than 1, it reflects that elements will segregate into the interdendritic region, which solidifies after the dendritic core. Along with segregation coefficients, the elemental composition of the dendritic core and interdendritic region of the WFZ are tabulated in Table 4.4.

$$\text{Segregation coefficient k} = \frac{C_S(\text{Solid})}{C_L(\text{Liquid})} \tag{4.1}$$

Table 4.4 : Segregation coefficient and elemental composition of different structures investigated in the WFZ

Spectrum	*Position*	*C*	*Al*	*Si*	*Ti*	*Cr*	*Mn*	*Fe*	*Ni*	*Nb*	*Mo*
EDS	Dendritic core (C_S)	34.78	0.20	0.08	0.58	14.08	0.75	31.04	18.41	0.08	-
	Interdendritic region (C_L)	10.36	0.28	0.18	0.58	15.41	0.71	56.17	16.02	0.29	-
	Segregation coefficient k	3.36	0.71	0.44	1	0.91	1.06	0.55	1.15	0.28	-
EPMA (WDS)	Dendritic core (C_S)	1.52	1.02	-	-	53.06	-	-	43.63	-	0.77
	Interdendritic region (C_L)	0.32	1.02	-	-	60.02	-	-	37.54	-	1.10
	Segregation coefficient k	4.68	1.00	-	-	0.88	-	-	1.16	-	0.70

The WFZ was mainly composed of Ni-rich Incoloy 800HT melt and had an FCC crystal structure (Palanivel et al., 2021). The FCC arrangement in Ni-based alloys provides lower diffusion rates of alloying elements, and due to this, microsegregation is promoted during weld solidification (Tan et al., 2011). So, it becomes necessary to investigate the extent of microsegregation in the WFZ. The PWHT specimen was utilized to observe the EDS and wavelength dispersive spectrometers (WDS) elemental composition results in dendritic cores and interdendritic regions of WFZ. EDS and WDS were taken at two different locations. WDS was assumed to give more accurate results. EDS results were taken only after confirming the repeatability and accuracy at different analyzed locations. Also, it helped in comparing the EDS and WDS data. From the elemental compositions obtained in EDS, segregation coefficients were calculated for the scanned elements using equation (4.1). The segregation coefficient for C, Ti, Mn, and Ni was greater than or equal to $k > 1$, suggesting that these elements must have remained in the solidified dendritic core (solid phase) (Yin et al., 2022). Ni does not strongly segregate into solid/liquid interfaces (BAL et al., 2018). Al, Si, Cr, Fe, and Nb had $k < 1$, confirming their possible segregation into interdendritic regions. The $k < 1$ for Fe was not a consistent observation as Fe does not segregate (DuPont, 2009). Fe diffusion was also observed in the area mapping; hence, the probability of segregation can be eliminated. Al and Ti are known to segregate extensively into interdendritic regions. Ti has been reported to segregate more vigorously than Al (DuPont, 2009). However, EDS data show Al segregated more as for lower k, but Ti deposition in SGB, SSGB, and the interdendritic region was witnessed in the WFZ. Al and Ti segregation also helps

in the precipitation of Ni_3Ti and Ni_3Al principal strengthening phase. Nb is preferred to segregate into the interdendritic region (Yin et al., 2022). Cr was also confirmed to segregate and must have led to the formation of carbides. The WDS results are more accurate and gave k > 1 for C, Al, and Ni, confirming that C and Ni were not segregated. C segregation could have been detrimental and severely affected the mechanical properties. However, Cr segregation could also have been detrimental, but EDS and WDS both gave k nearer 1 for Cr; hence, its segregation was not extensive. Al had k = 1, but its segregation is highly probable. Mo also had k lesser than 1 in WDS results and its segregation into interdendritic region was confirmed. Mo segregation leads to the formation of MoC carbides which provides precipitation hardening in the region (Dak and Pandey, 2021). Microsegregation under rapid cooling rates is also responsible for forming undesirable phases at the end of the solidification of the interdendritic region in the WFZ.

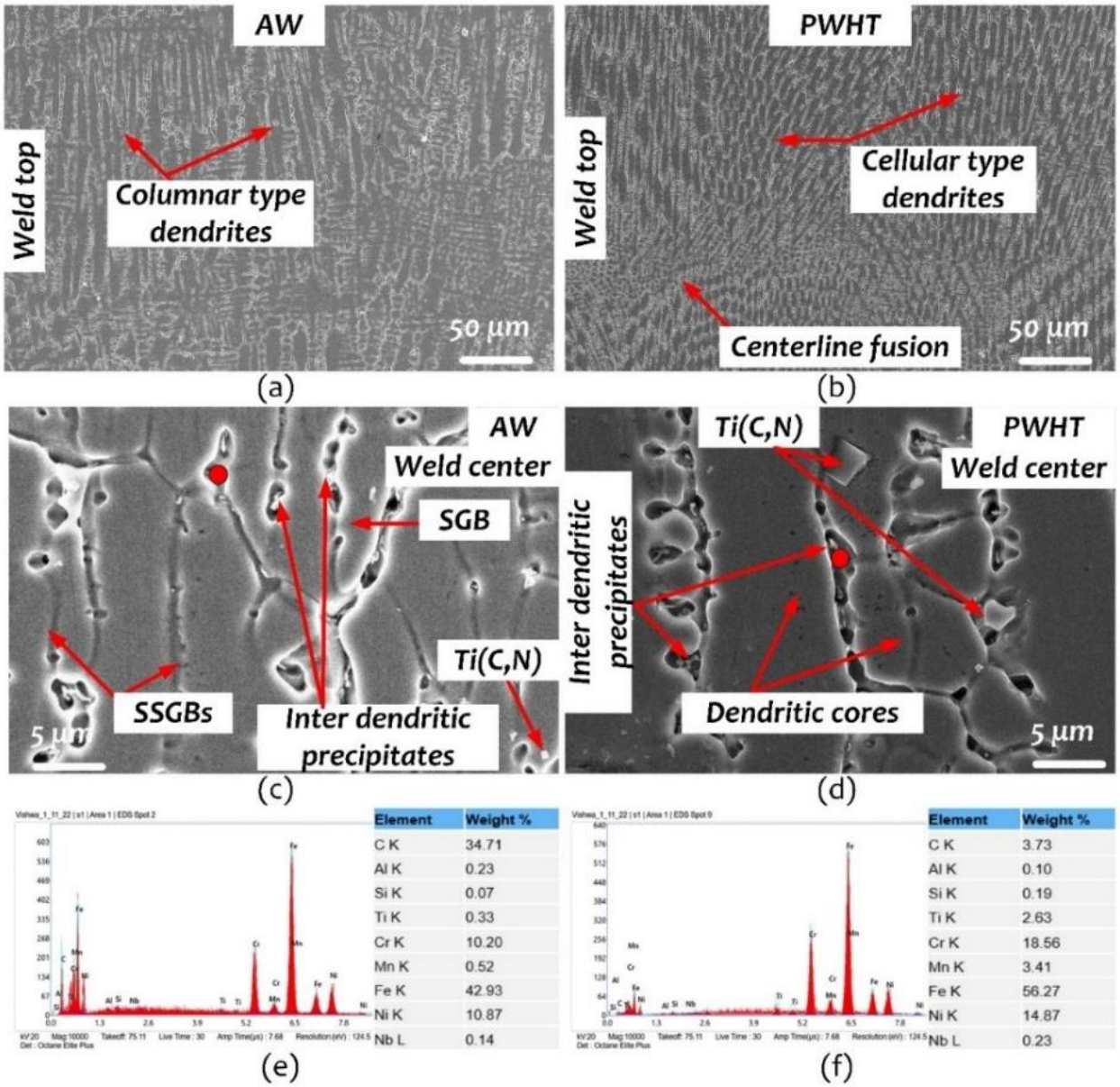


Figure 4.22 : FESEM micrograph and EDS spectrum of (a) WFZ in AW state (b) WFZ in PWHT state (c) dendrites in AW state WFZ (d) dendrites in PWHT state WFZ (e) elemental composition of spotted interdendritic particles in AW states WFZ (f) elemental composition of spotted interdendritic particles in PWHT states WFZ

4.2.3 Tensile Properties

The tensile specimens displayed in Figure 4.23(a), are the specimens that fractured as a result of the tensile test. During the testing and comparison process, the specimens were both at AW and PWHT conditions. For the purpose of determining the WFZ's tensile strength, the subsize specimens were made. According to the results of the tests, the Incoloy 800HT weld

interface was the weakest link. The tensile test results are summarized in Table 4.5. The ultimate tensile strength (UTS) of the AW and PWHT state standard specimens was almost identical, measuring 550 MPa and 549 MPa, respectively. Their yield strengths, measured in megapascals (MPa), were 241 and 231, respectively. The crack in both specimens began at the Incoloy 800HT weld interface and then moved toward the Incoloy 800HT HAZ. According to what has been seen, the development of secondary phases in the TZ and the coarsening of precipitates that were already present in the HAZ grains close to the Incoloy 800HT weld interface may have contributed to the nucleation and growth of the fracture. Also, a Type II boundary may have acted as a crack nucleation site. The Ti deposition near the HAZ grain boundaries forms the low melting precipitates, and with grain boundary thickening, it could have affected and deteriorated the strength. The PWHT did not affect the strength since Incoloy 800HT does not react to PWHT. Additionally, comparable elongation percentages (31% and 32%) and area reduction percentages (44% and 41%) were discovered for the AW and PWHT state standard specimens, respectively. The ultimate tensile strength of the subsize tensile specimens measured 562 MPa in the AW state and 592 MPa in the PWHT condition. The AW subsize specimen failed in a manner that was comparable to that of the standard specimen. PWHT subsize specimen failed from the WFZ. The WFZ in PWHT had UTS almost equal to that of Incoloy 800HT base metal. The Incoloy 800HT is highly prone to sensitization, leading to intergranular cracking. Ti accumulation near the HAZ grain boundaries is also related to Cr activity and diffusion. Slight Cr enrichment can promote carbide formation (Yang et al., 2022). Intergranular failure is highly probable if Ti depletes from the matrix, which restricts the principal strengthening gamma prime phase formation (Bhaduri et al., 1995). The stress-strain engineering plots for the performed tensile test are shown in Figure 4.23(b).

Further, a fractography study was conducted to confirm the mode of fracture. Figure 4.24(a-d) shows the fractured surface micrographs of standard AW, standard PWHT, subsize AW, and subsize PWHT specimens, respectively. Figure 4.24(a) shows tear ridges and macro dimples, suggesting a mixed failure mode in the AW standard tensile specimen. The macro voids were present as microvoids must have combined and started the nucleation of the fracture. Figure 4.24(b) confirms the ductile failure mode in the PWHT standard tensile specimen, as dimples were present in the majority, and inclusions were also spotted, which could be the gamma prime phase at the grain boundary. The AW subsize tensile specimen (Figure 4.24(c)) had a mixed failure mode with cleavage facets along the dimples. The significant presence of cleavage facets hints that fracture propagated along this path, possibly the Incoloy 800HT weld interface. The PWHT subsize tensile specimen fractured surface in Figure 4.24(d) was witnessed with dimples and cleavage facets confirming the ductile nature of the WFZ and mixed mode of failure.

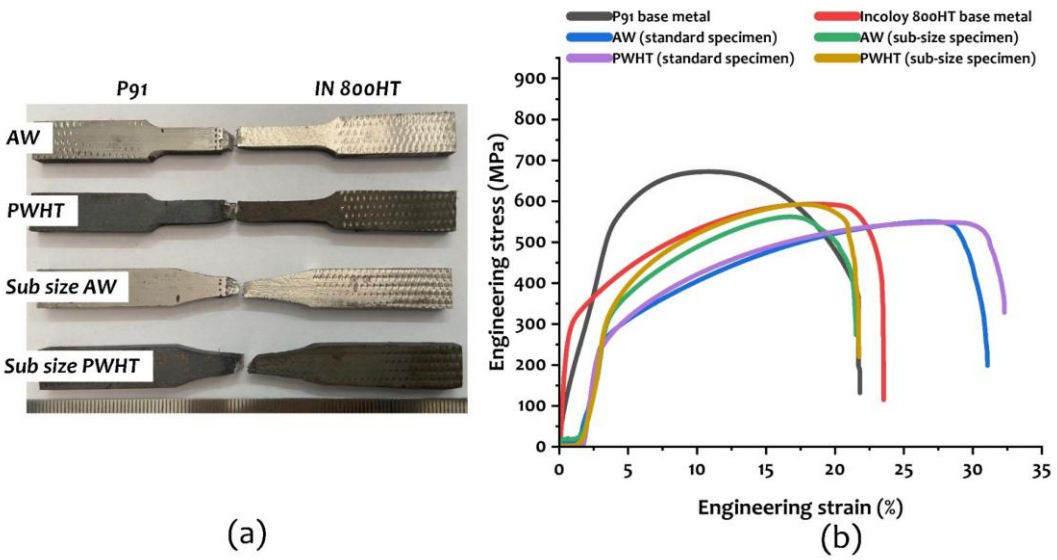


Figure 4.23 : (a) Fractured tensile specimens after testing and (b) plotted engineering stress-strain curves for base metals and tested tensile specimens

Table 4.5 : Tensile properties of different weld specimens

Specimens	*UTS (MPa)*	*YS [offset 0.2%] (MPa)*	*Elongation (%)*	*Reduction in the area (%)*	*Failure site*
AW (Standard specimen)	550 ± 5	241 ± 5	31 ± 2	44 ± 2	Near Incoloy 800HT interface
AW (Subsize specimen)	562 ± 5	-	22 ± 2	59 ± 3	Near Incoloy 800HT interface
PWHT (Standard specimen)	549 ± 5	231 ± 6	32 ± 2	41 ± 3	Near Incoloy 800HT interface
PWHT (Subsize specimen)	592 ± 5	-	21 ± 3	57 ± 3	WFZ

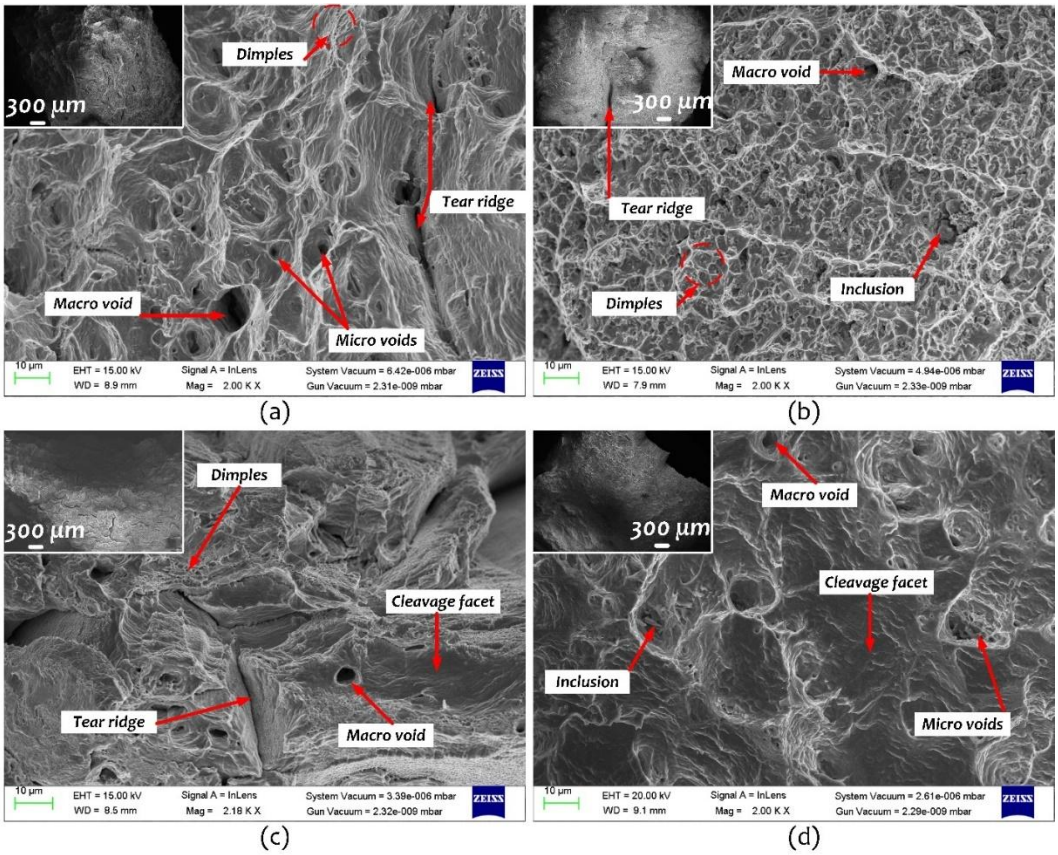


Figure 4.24 : Fractography SEM micrographs of (a) AW state standard tensile specimen (b) PWHT state standard tensile specimen (c) AW state subsize tensile specimen (d) PWHT state subsize tensile specimen

4.2.4 Microhardness Properties

The Vickers microhardness idents were taken on the etched metallographic specimens, as shown in Figure 4.25. The array of indents was taken at a gap of at least 1 mm from the specimen edges. The indents in the transverse cross-section direction were taken 0.25 mm apart to characterize the narrower regions of the WFZ and HAZ. The rows of indents were spaced at a 0.5 mm distance. The microhardness observations helped gauge the effects of metallurgical changes during welding. As the formation of different phases during the welding and stresses induced to affect the strength of the material, microhardness analysis helped characterize and identify corresponding regions.

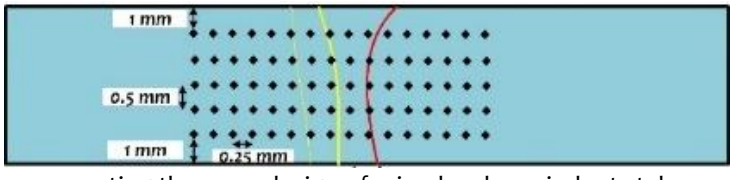


Figure 4.25 : Schematic representing the array design of microhardness indents taken

The 2D contour plots were produced in the OriginPro 2022b software. Figure 4.26 demonstrates the variation in microhardness along and across the weld in its AW state. For the AW state specimen, the variance can be seen quite plainly across a distance of less than one millimeter in the HAZ region. The CGHAZ region with the highest microhardness can be found in red and orange colors on the contour plot along the P91 weld interface. From CGHAZ to ICHAZ, the color gradients were found to decrease gradually and match with base metal readings. The ICHAZ was not observed with any detrimental decrease in microhardness. The lowest value for ICHAZ recorded was 234 HV. In the vicinity of the weld top region, it was noticed that the CGHAZ reached a peak value of 546 HV. It was determined that the FGHAZ had an average microhardness value of approximately 442 ± 15 HV. The increase in microhardness that may be observed in FGHAZ and CGHAZ regions is entirely attributable to the precipitates' partial dissolution (Kumar and Pandey, 2022). The WFZ had a microhardness distribution that was consistent throughout and had an average of 242 ± 15 HV. The microhardness of the Incoloy 800HT HAZ in its AW form averaged out to be 245 ± 15 HV. WFZ had comparable microhardness characteristics as of Incoloy 800HT, and the HAZ region of Incoloy 800HT did not go through any notable phase changes during welding. The base metal region of Incoloy 800HT had an average microhardness of 246 ± 15 HV, which was identical to the HAZ region and WFZ. This suggests that WFZ had similar microhardness characteristics as Incoloy 800HT. The P91 base metal side of the AW specimen has an average microhardness of 260 ± 15 HV. The weld interface of the Incoloy 800HT was observed to have a microhardness of 236 HV.

In contrast, the P91 weld interface had an average and peak microhardness of 442 ± 5 HV and 503 HV, respectively. The evolution of untempered martensite at the weld interface was the cause of such a high level of microhardness at the P91 interface. The contour profile across the weld shows a rise in microhardness in the P91 HAZ region and is kept constant along the remaining region. The contour profile line along the WFZ also showed a homogenous nature and distribution of microhardness.

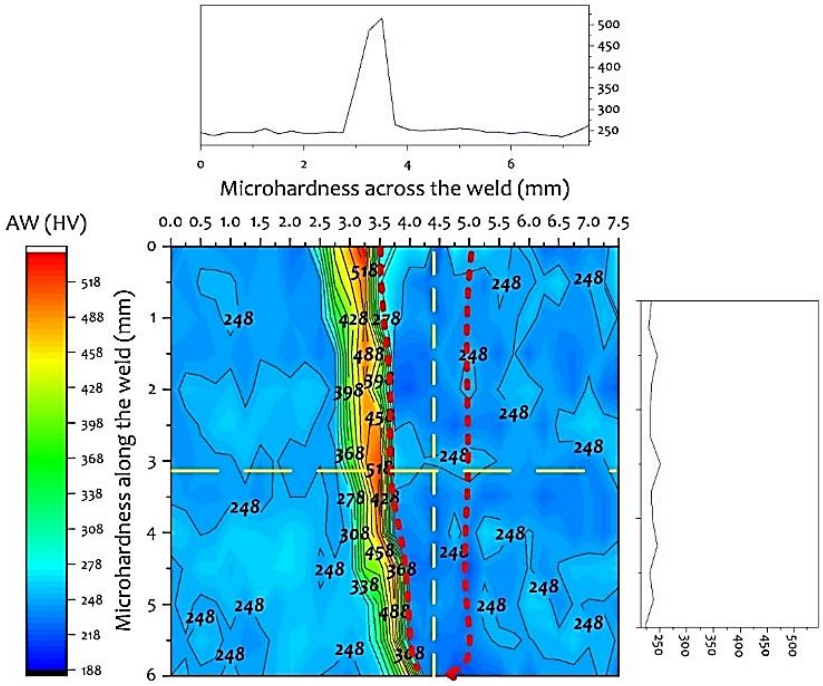


Figure 4.26 : 2D Microhardness contour profile plot of AW specimen

Further, specimen in the PWHT state was also studied similarly. The 2D contour map of microhardness observed in the PWHT specimen is shown in Figure 4.27. PWHT is recommended for tempering the microstructure and re-evolution of dissolved precipitates. PWHT has also been observed to produce a positive effect on toughness. The CGHAZ was observed with a drastic reduction in microhardness to 247 ± 15 HV. The microhardness was found to reduce most in the CGHAZ region, which was found to be located below the weld center. On the other hand, the

CGHAZ region that was found to be located above the weld center and significantly close to the weld top region was found to have a peak microhardness of 441 HV. This could be because P91 must have melted more near the weld top region at the weld interface, as during EBW, the maximum temperature is obtained near the surface, and this is sufficient enough to melt P91 into the weld. The CGHAZ region in the vicinity of the weld top region was not observed with any severe drop in microhardness, and this could be because P91 must have melted more near the weld top region at the weld interface. However, both untempered martensite and tempered martensite were only found in a narrow area close to the P91 weld interface. In addition, the microhardness of the FGHAZ area decreased to an average of 246 ± 20 HV. It was determined that there was an increase in the levels of microhardness in the ICHAZ region, and the average level of microhardness in the ICHAZ region was 246 ± 10 HV. Resurfacing carbide precipitates during the tempering process resulted in a homogenization of the P91 HAZ microhardness.

Interestingly, in the WFZ after PWHT, a reduction in microhardness was observed, and the average dropped to 222 ± 15 HV. Additionally, the Incoloy 800HT HAZ and base metal region had a decrease in the average microhardness of 218 ± 20 HV and 224 ± 15 HV, respectively. Since the PWHT temperature of 760 ℃ and the period of 2 hours is enough for precipitation of the Cr-rich $M_{23}C_6$ phase. The $M_{23}C_6$ must have precipitated in the WFZ and Incoloy 800HT region, reflecting a minor decrease in microhardness (Thakare et al., 2019). The microhardness of the P91 weld interface was 285 HV at the top weld region and 264 HV in the area that was closest to the weld root region. While there was no such significant variation along the Incoloy 800HT weld interface, the microhardness at the Incoloy 800HT weld interface in the PWHT state was 220 ± 5 HV. The contour profile lines across the weld and along the WFZ showed an almost homogenized trend. It was difficult to remark on the Incoloy 800HT weld interface since it has not demonstrated any substantial microhardness variation. As a result, the microhardness of the region could not justify the tensile failure that occurred from the Incoloy 800HT weld interface. In a study conducted where P91 and Incoloy 800HT were joined using an arc welding process and different Ni-based fillers. However, the arc welding process reportedly produced a wider HAZ region, and CGHAZ peak microhardness was also comparatively less with respect to the microhardness observed for the current weldment.

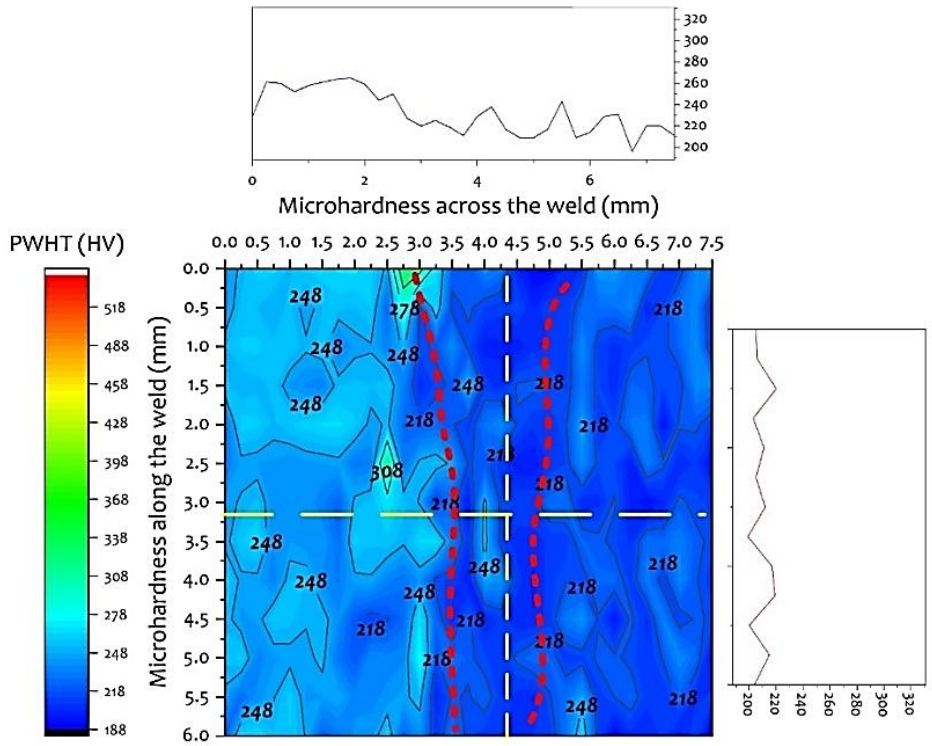


Figure 4.27 : 2D contour profile plot of microhardness across the specimen in PWHT state

4.2.5 Charpy Impact Toughness

Both AW and PWHT specimens were tested for their Charpy impact toughness using the V-notched method. The prepared specimens are displayed in Figure 4.28(a), and in Figure 4.28(b), the broken specimens are displayed. The AW specimen had a Charpy impact toughness value of 63 J, and the presence of shear lips and lateral expansion of 2.5 mm confirmed the ductile mode of failure. The path fracture was also along the WFZ. The PWHT specimen, on the other hand, only demonstrated a marginal improvement in Charpy impact toughness, reaching 69 J. PWHT did not fracture completely, but no deviation in fracture was observed. The slight increase in toughness could be due to carbide precipitation in the WFZ, which helped pin down the grain boundaries and dislocations (Anand et al., 2016). PWHT specimen also had shear lips formation and lateral expansion of around 1.8 mm. Compared to the Charpy impact toughness of P91 (102 J) and Incoloy 800HT (110 J), both specimens had a significantly lower Charpy impact toughness than the base metals. The EBW dissimilar weld Charpy impact toughness also qualified the minimum benchmarked Charpy impact toughness limits. Typically, dissimilar metals have thermal expansion coefficients and solidification behaviors. The quick cooling during electron beam welding might result in the dissimilar metals not solidifying evenly. It can lead to the production of microstructural defects such as cracks and intermetallic compounds. The uneven distribution of alloying materials that might occur due to microsegregation can lead to the formation of a microstructure with changing characteristics in the weld fusion zone. Because of the microstructural heterogeneity, different weld zones might have varying degrees of hardness, strength, and toughness. These different variances in mechanical properties can result in stress concentrations and the beginning of cracks, which in turn results in a reduction in the Charpy impact toughness of the material. Figure 4.28(c-d) shows the fractography micrographs of the broken AW and PWHT specimen surfaces, respectively. Both micrographs showed a consistent distribution of dimples, which is an important factor in preventing fracture propagation. The cleavage facets were also present, confirming the hybrid fracture mode but ductile dominantly. The low Charpy impact toughness and hybrid mode failure could be due to the formation of fusion centerline and columnar dendrites in its vicinity. The fusion centerline and columnar dendrites must have provided an easy path for fracture propagation. (Sims et al., 1987) also agreed with the results that precipitation of $M_{23}C_6$ carbides could enhance the mechanical properties of a Ni-based alloy.

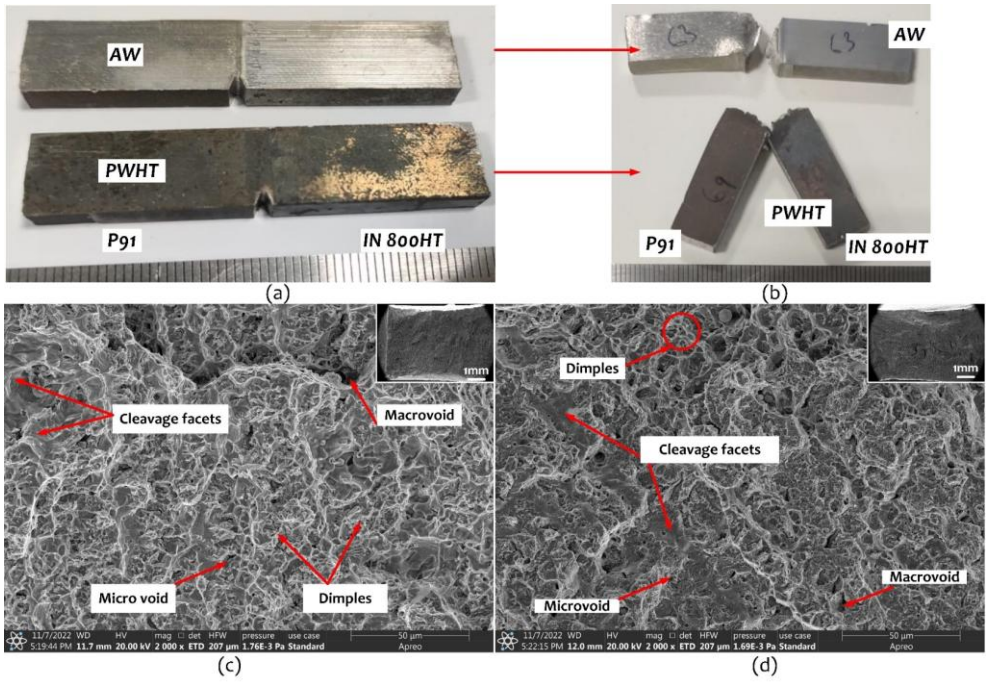


Figure 4.28 : V-notched Charpy impact toughness specimens (a) before testing (b) after testing; Fractography FESEM micrographs of (c) AW state fracture surface and (d) PWHT state fracture surface

4.3 AUTOGENOUS TUNGSTEN INERT GAS (TIG) WELDING WITH INTERLAYERS

4.3.1 Macroscopic Observations

The functionally graded joint between P91 steel and Incoloy 800HT was developed using interlayers of Incoloy 800HT, Inconel 617, and P91 steel. The interlayer strips were of 1 mm width, and their arrangement is shown in Figure 4.29(a). The autonomous-TIG welding pass was performed on both sides of the plates on a special-purpose semi-automated welding table, as shown in Figure 4.29(b). The macrograph of the weld bean obtained is shown in Figure 4.29(c). As observed from the micrograph, the weld bead width at the approximate weld center was 13.4 mm, while the maximum was 18.7 mm. The sequence of welding passes performed has also been indicated in Figure 4.29(c). The interlayers were inserted in this particular sequence so as to provide a balanced transition of thermal expansion at elevated temperatures during the welding. The Inconel 617 interlayer acted as an intermediator between P91 and Incoloy 800HT and also imparted strength to the DWJ. The HAZ of the P91 steel side was around 11.3 m wide near the weld center, as it undergoes intricate microstructural changes due to the thermal cycles experienced during welding. Further, no macroscopic defects such as solidification cracking, porosities, inclusions, and lack of fusion were detected in the macroscopic observations.

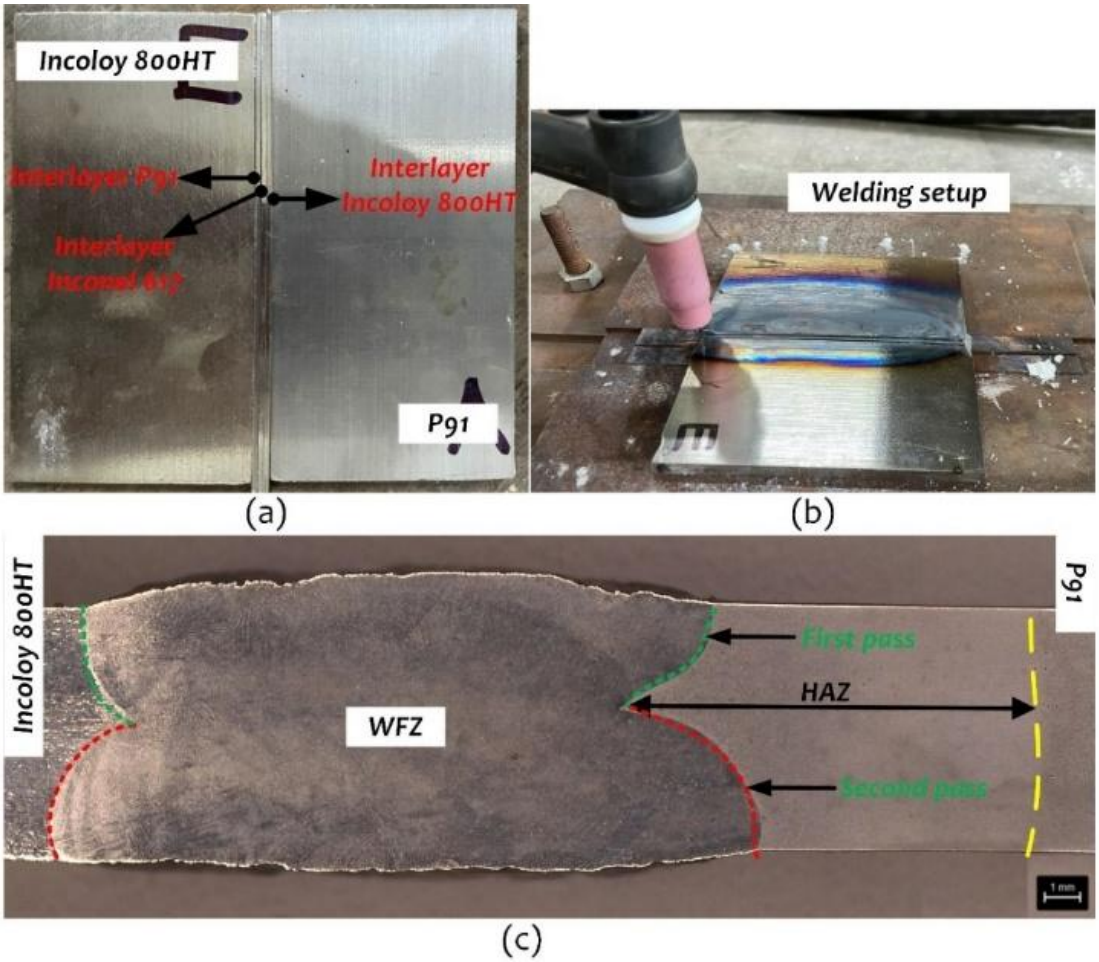


Figure 4.29 : (a) Interlayers placement before welding (b) welding setup (c) weld macrograph

4.3.2 Heat Affected Zone (HAZ)

In the current weldment, compared to previously developed P91 HAZs (section 4.1.2) similar features were observed without any significant development. Hence, discussion again is not necessary, though the optical and FESEM micrographs of CGHAZ, FGHAZ, and ICHAZ formed for current weldment are shown in Figure 4.30 (a-c). Though slight changes in grain size were observed, as in CGHAZ, larger coarse grains were observed. The grain size observed in the CGHAZ was around 35 ± 10 μm, FGHAZ was around 10 ± 10 μm, and ICHAZ was around 12 ± 10 μm

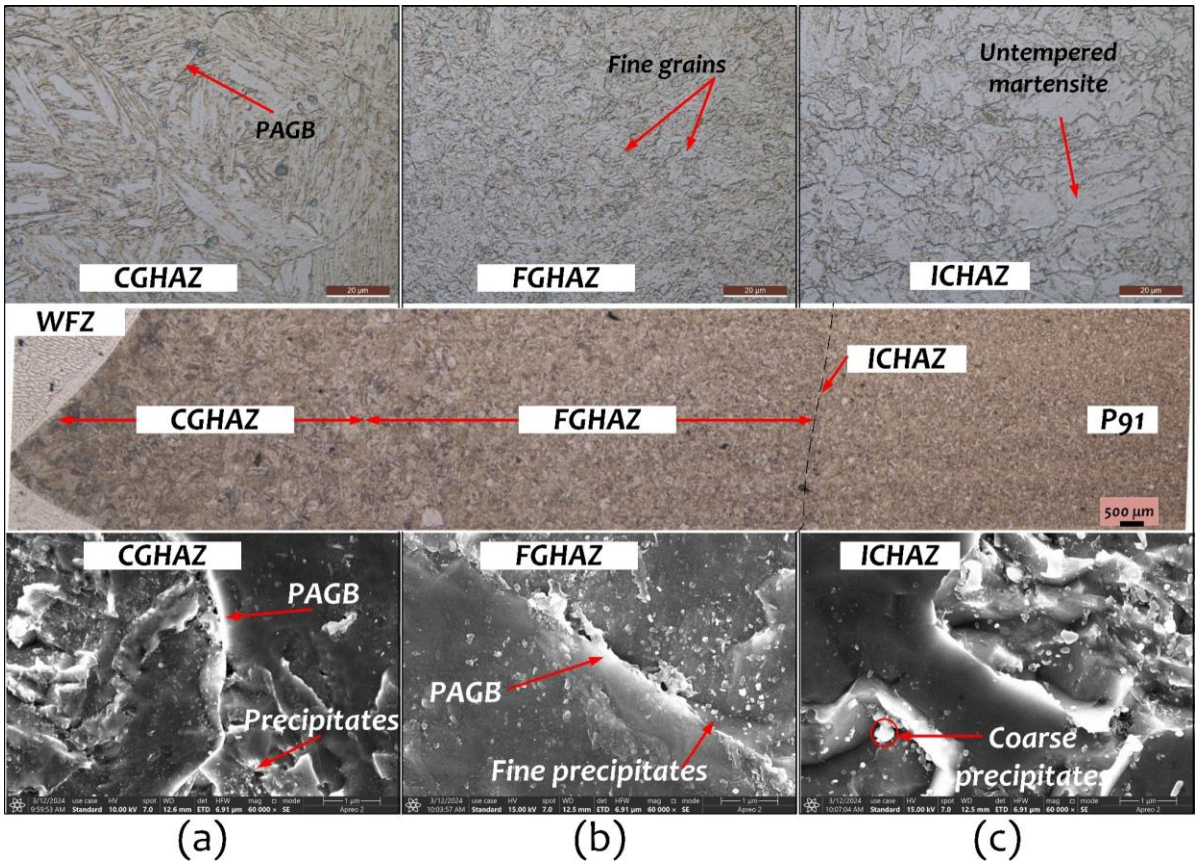


Figure 4.30 : Micrographs of (a) CGHAZ (b) FGHAZ (c) ICHAZ

The Incoloy 800HT HAZ region was quite narrow. The grain size was stable and was observed with significant changes. Austenite grain boundaries were heavily coarsened and sensitized only in the HAZ region just near the weld interface. Figure 4.31 clearly shows the grain coarsening in the Incoloy 800HT HAZ region. The grain size observed in the Incoloy 800 HT HAZ was around 272 ± 10 µm Also, the boundaries were heavily enriched with Ti, as confirmed with the EDS. This is due to the complexities of microsegregation during solidification, especially due to the presence of adjacent P91 interlayer. The contract difference in the compositions must have generated a gradient leading to the accumulation of Ti at the austenitic grain boundaries. This phenomenon has also been reported in the past and is of great concern when Incoloy 800HT is involved (Shah Hosseini et al., 2011).

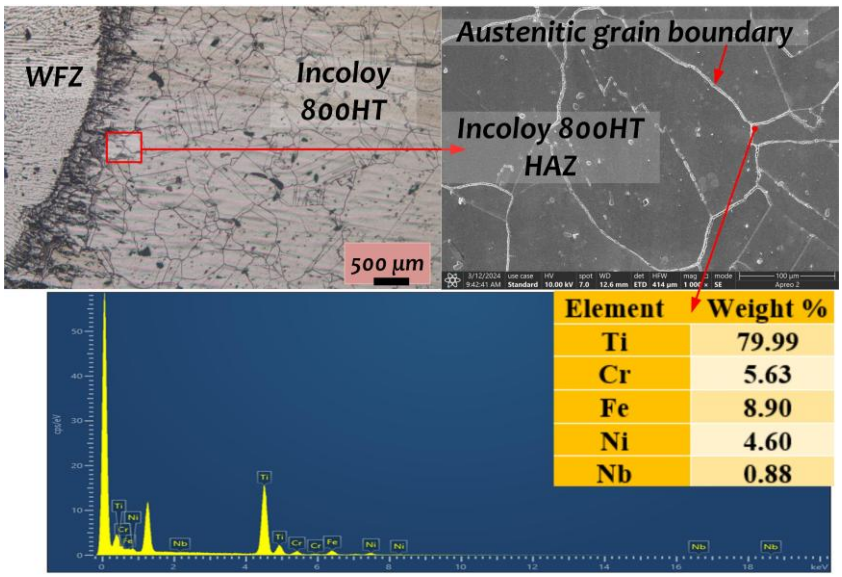


Figure 4.31 : Micrographs of Incoloy 800HT HAZ with EDS

4.3.3 Weld Interface and Weld Fusion Zone (WFZ) Microstructure Characterization

The complete WFZ is shown in Figure 4.32(a-c). The weld region (Figure 4.32(a)) near the Incoloy 800HT weld interface had a prominent presence of columnar dendritic growth. The region was also enriched with heavily coarsened precipitates near the SGBs. The precipitates in the interdendritic regions were Ti-rich. The accumulation of Ti along this region generates stresses and supports the formation of cracks (Sayiram and Arivazhagan, 2015). The weld region in the center (Figure 4.32(b)) shows the dominant presence of cellular structures; the presence of Inconel 617 interlayer in the center plays an important role in providing finer structure and functional grading to the WFZ. The precipitates in the center were also found to be Ti-rich. The weld region near the P91 weld interface also had the presence of columnar and cellular structures. The columnar dendrites were formed in the initial phases of solidification at the weld interface. Again, the region was found with Ti-rich phases along the SSGBs and dendritic cores. The EDS hints at the smooth transition in the chemical composition of the WFZ. The interlayers are said to control carbon migration and restrict the formation of carbon-enriched or carbon-denuded zones (Kulkarni et al., 2021). The dilution of interlayers successfully helped in achieving the function grading and a complete austenitic mode of solidification was observed. The P91 weld interface was observed with competitive growth of dendrites into the WFZ. The line mapping in Figure 4.33 shows the variation of allying elements composition such as for Fe, Cr, Ni, and Nb. Similarly, variation was observed for the Incoloy 800HT weld interface (Figure 4.34) for elements such as Fe, Cr, Ni, and Mo. A sudden peak of Ti observed is due to the presence of the Ti-rich element in the region. No significant diffusion or segregation was observed across the weld interface.

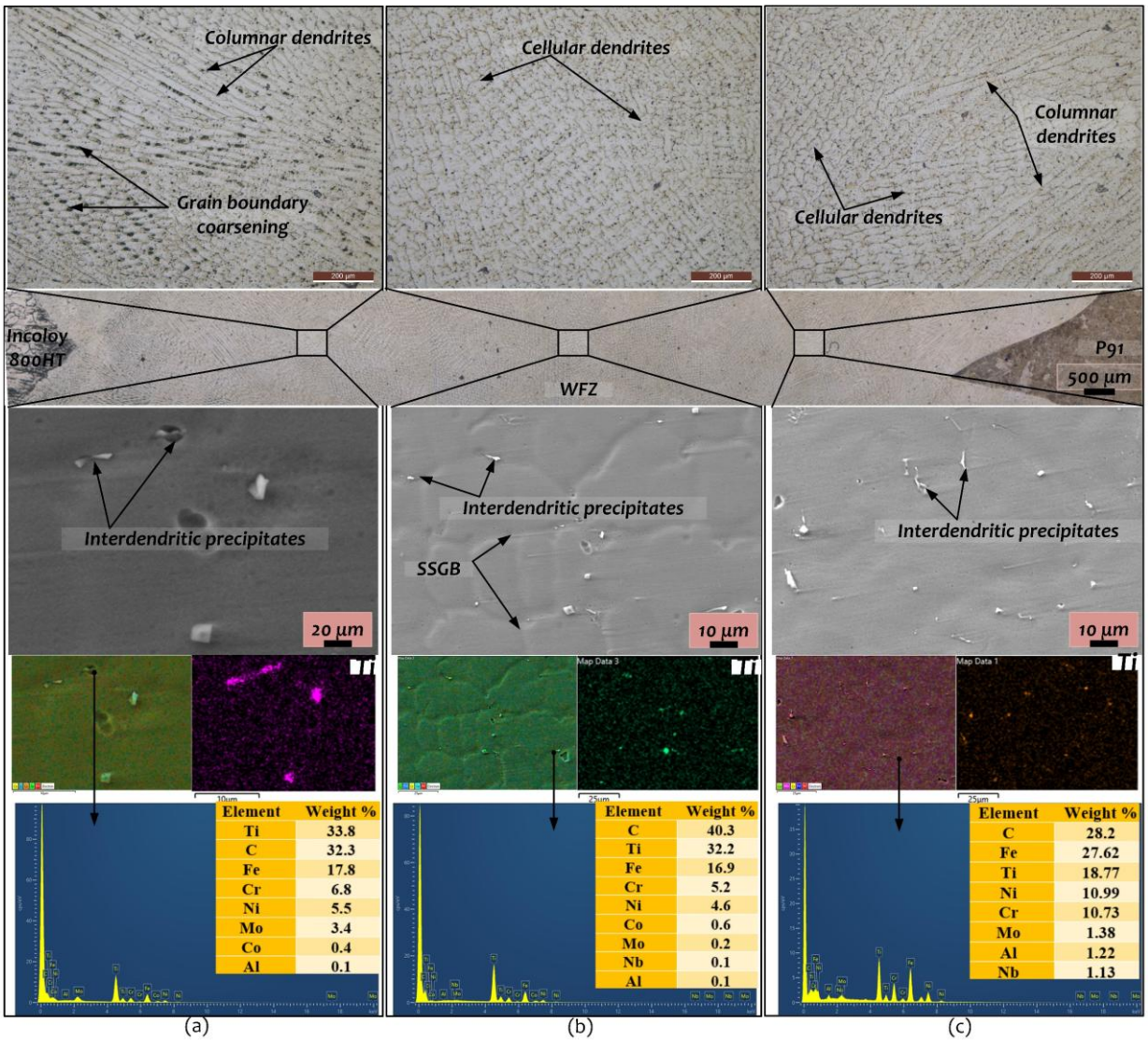


Figure 4.32 : Micrographs of different WFZ areas (a) Near Incoloy 800HT weld interface (b) near weld center (c) near P91 weld interface

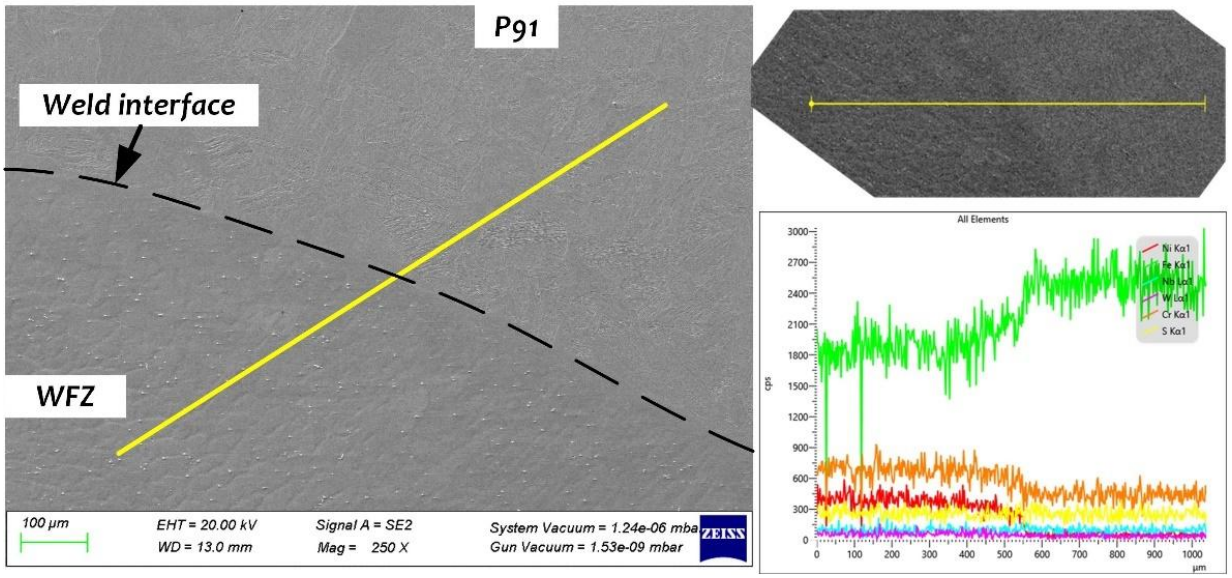


Figure 4.33 : Micrograph of P91 weld interface with line mapping

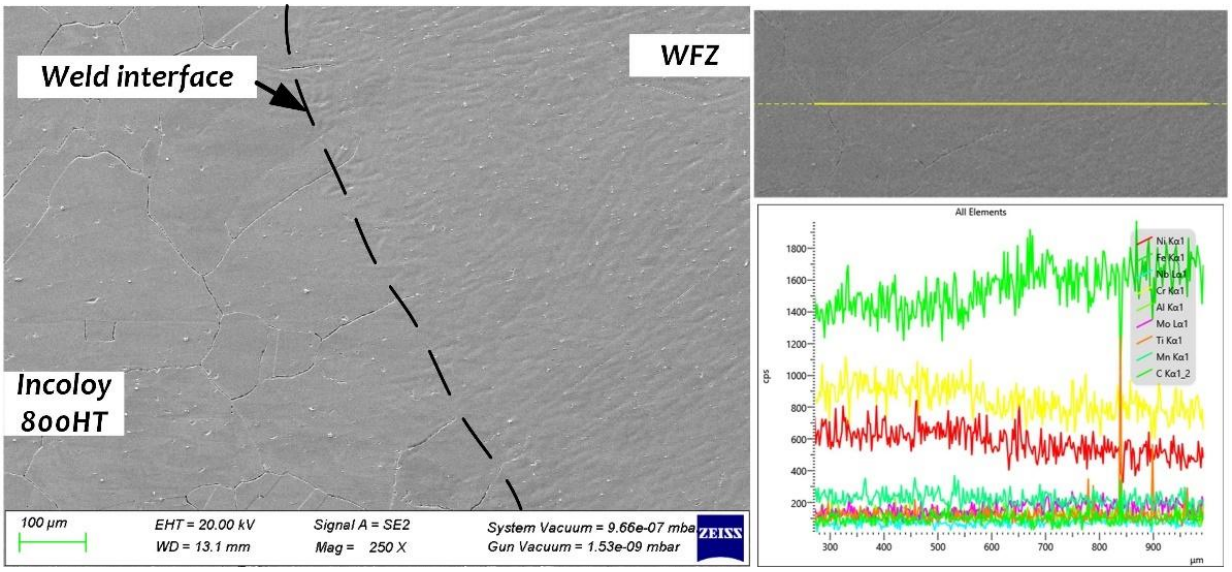


Figure 4.34 : Micrograph of Incoloy 800HT weld interface with line mapping

4.3.4 Tensile Properties

Figure 4.35(a) displays the specimen in a broken condition following the completion of the testing. Table 4.6 presents a summary of the tensile properties observed during the conducted tests. The flat AW standard specimen from the WFZ. The specimen had an ultimate tensile strength (UTS) of 460 ± 5 MPa. The specimen had elongation measurements of 34%. Figure 4.35(a) clearly depicts the elongation marks in the WFZ and Incoloy 800HT base metal, showing significant ductile behavior. However, after severe plastic deformation in the WFZ, the crack initiated in the WFZ near the Incoloy 800HT weld interface where P91 interlayers were placed, and heavy accumulation of Ti was detected at the SSGBs in that particular region. The Ti-rich phases in the interdendritic regions provided nucleation sited for cracks during the deformation. Precipitates can hinder the motion of dislocations and enhance the material's capacity to undergo plastic deformation. It is crucial to have a thorough understanding of the local metallurgical changes that occur during the welding thermal cycle. This is evident from the complex microstructure and variations in mechanical properties in the evolved WFZ matrix. The specimen displays ductile behavior, as evidenced by the fractured surface. The flat AW specimen, as depicted in Figure 4.35(b), displays a fracture that is a combination of both ductile and brittle fractures. However, the primary mode of fracture is ductile. Furthermore, it was observed that there were cleavage facets. The fragility of the material can be ascribed to the accumulation of

stress surrounding any secondary phases that have developed in the WFZ. These secondary phases may have served as places where microcracks might form through nucleation. In addition, the formation of larger secondary phases within the matrix made it easier for cracks to spread along the crystal lattice's less resistant planes. Furthermore, as the size of the grains grows as a result of coarsening, the grain boundaries act as locations where the nucleation of voids begins.

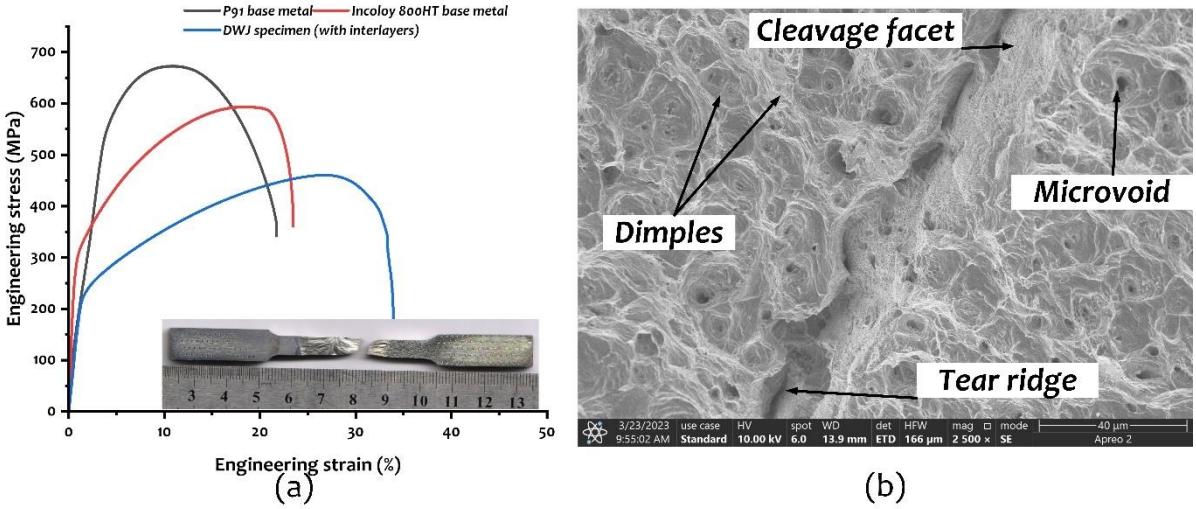


Figure 4.35 : (a) Stress-strain plots (b) fractured surface micrograph

Table 4.6 : Tensile properties of different weld specimens

Specimens	*UTS (MPa)*	*YS [offset 0.2%] (MPa)*	*Elongation (%)*	*Reduction in the area (%)*	*Failure site*
AW (Standard specimen)	460 ± 5	211 ± 5	34 ± 2	46 ± 2	In WFZ

4.3.5 Microhardness Properties

Microhardness tests were performed across the cross-section of the DWJ weld bead. The indents were measured using a 0.5mm spacing, as shown in the schematic diagram presented in Figure 4.36. There was a significant difference in the microhardness found in the P91 HAZ of the DWJ. In the CGHAZ region, the microhardness peaked at 411 HV, whereas the ICHAZ zone recorded the lowest microhardness at 195 HV. In the P91 HAZ region, there was a distinct area called FGHAZ, which had an average microhardness of 395 ± 10 HV. The WFZ exhibited a microhardness of approximately 168 ± 5 HV. A value of 174 HV was recorded near the center of the WFZ, which is the highest recorded. The microstructure of the Incoloy 800HT HAZ remained to show some increment due to precipitate hardening the austenitic grain boundaries. The hardness recorded in the Incoloy 800HT HAZ region was 212 HV. This is slightly higher than the 180 ± 10 HV average microhardness observed on the 800HT base metal side. The region of the Incoloy 800HT weld interface saw a low of 169 HV due to the formation of complex phases in the region. The CGHAZ in the P91 HAZ showed higher microhardness levels due to the formation of untempered martensite. The ICHAZ drop happened due to the presence of martensite that had been heat-treated too much in that particular area. The WFZ was observed with a gradually increasing trend in microhardness, with the highest near the P91 weld interface. This suggests that the interlayers are diluted and mixed completely, providing a smooth transition and functional grading effect. Further investigation is needed to understand the impact of post weld heat treatment on the interlayer welding technique.

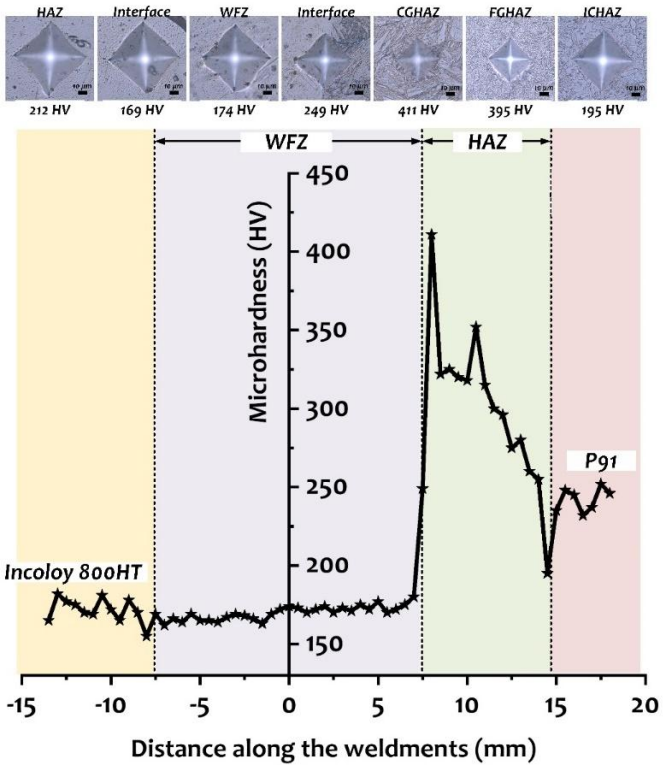
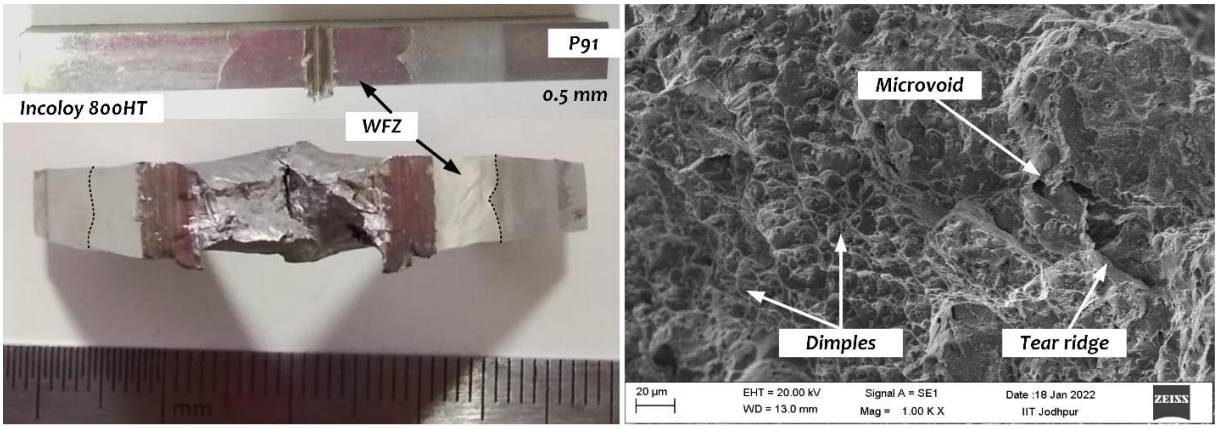


Figure 4.36 : Microhardness variation plot

4.3.6 Charpy Impact Toughness

Figure 4.37(a) shows the fractured sample after the impact. It was observed that the AW specimen experienced a highly ductile failure process, indicated by the presence of shear lips and lateral expansion. The fracture extended solely along the WFZ. The specimen displayed a Charpy impact toughness rating of 95 ± 5 J. The Charpy impact toughness for the DWJ fabricated qualified as per the set standards.

The analysis of the fractured surface in the WFZ revealed a hybrid failure mode, as depicted in Figure 4.37(b). The specimen exhibited a dominant ductile behavior characterized by lateral contraction and the presence of dimples. Confirming the hybrid failure mode on impact is indicated by the presence of cleavage facets and tear ridge. The high Charpy impact toughness and predominant ductile behavior can be attributed to the development of an austenitic structure and the presence of multiple slip systems in the fcc phase observed in the WFZ.



(a) (b)

Figure 4.37 : (a) Tested specimen for Charpy impact toughness (b) fractured surface micrograph